Proceedings 10th NUMGE 2023
10th European Conference on Numerical Methods in Geotechnical Engineering
Zdravkovic L, Kontoe S, Taborda DMG, Tsiampousi A (eds)

https://doi.org/10.53243/NUMGE2023-437

On the application of constitutive models with an emphasis on offshore engineering problems

A. Grammatikopoulou[1], F.C. Schroeder[1], E. Sailer [2], D.M.G. Taborda[3], D.M. Potts[3]

[1]*Geotechnical Consulting Group, London, UK*
[2]*formerly Geotechnical Consulting Group, London, UK*
[3]*Imperial College, London, UK*

ABSTRACT: Numerical analysis is increasingly being used in the development of geotechnical design methodologies and in their application in practice. The results of any numerical analysis depend critically on the constitutive models chosen to represent the soils and the parameters adopted to model their response. This paper presents an overview of the authors' experience in the application of constitutive models to simulate the response of soils that are commonly encountered in offshore engineering problems and specifically offshore wind farm sites. The paper is divided in two parts. The first part studies the modelling of sand deposits with varying density, using two elasto-plastic constitutive models, i.e. a state parameter-dependent constitutive model based on the Mohr-Coulomb failure criterion (Taborda et al., 2018) and a strain softening Mohr-Coulomb model (Potts et al. 1990). It details the derivation of model parameters and calibration of the models, on the basis of commercial high-quality in-situ and laboratory test data, and compares the models' predictions in the analysis of an example monopile foundation. The second part examines the modelling of stiff clays. Particular attention is paid to the influence of plasticity on the clays' response. The paper highlights the challenges in choosing appropriate models and model parameters to match the response measured as part of high-quality ground investigations.

Keywords: Constitutive modelling; finite element analysis; monopile foundations; offshore wind farms

1 INTRODUCTION

Over the last decades laboratory and field techniques have become more sophisticated and so has the development and application of constitutive models used to simulate the response of soils in numerical analysis. In addition, numerical analysis is increasingly being used as a tool in the development of design methodologies, as well as in their application in practice.

For example, the PISA design methodology (Burd et al., 2020, Byron et al., 2020), which has led to significant advances in the design of offshore monopile foundations, was developed on the basis of sophisticated 3D finite element (FE) analyses carried out with the Imperial College finite element code ICFEP (Potts and Zdravkovic, 1999). The ability of the FE method to deliver greatly improved monopile response predictions was demonstrated by the close agreement achieved between Class A predictions (i.e. predictions made before the corresponding field measurements, Lambe, 1973) and the outcome of large scale field tests on monopiles subjected to lateral and moment loading at two sites; i.e. Cowden, a glacial clay till site (Zdravkovic et al., 2020b), and Dunkirk, a marine sand site (Taborda et al., 2020).

The success of the Class A predictions was facilitated by an accurate characterisation of the ground conditions at the two sites (Zdravkovic et al., 2020a), through the interpretation of high-quality ground investigation information, and the application of sophisticated constitutive models calibrated to accurately replicate the measured soil response at an element level.

This paper presents an overview of the authors' experience in the application of constitutive models to simulate the response of materials that are commonly encountered in offshore wind farm sites (OWFs). This has included interpretation of high-quality ground investigation information, comprising in-situ and advanced laboratory testing, choice of appropriate constitutive models to simulate the response of the materials encountered, calibration of the models on the basis of in-situ and laboratory tests from across wind farm sites and application of the models in 3D FE analyses of monopile foundations supporting individual Wind Turbine Generators (WTGs).

According to the numerical-based PISA methodology, advanced 3D FE analyses are carried out at specific key monopile locations across a wind farm. On the basis of these analyses four sets of location specific soil reaction curves are extracted for each material encountered. These are then parameterised and subsequently utilised in simpler 1D Winkler-type beam-spring models applied

at every WTG location, as part of a large number of optimisation calculations employed during the monopile design process. As such the 3D FE analyses, and in turn the constitutive models employed in these analyses, play a crucial role in the application of the PISA design methodology in practice.

Offshore sites often cover areas which tend to be significantly larger than typical onshore sites and their dimensions are often measured in kilometres, rather than tens or hundreds of meters. As such, the variability of the materials encountered can often be greater than at onshore sites. This poses obvious challenges in the choice, calibration and application of the appropriate constitutive models. Moreover, the philosophy behind the ground investigation strategies of offshore wind farm sites tends to be different to that for typical onshore sites. The latter usually comprises relatively closely spaced boreholes which cover the whole development area. In the case of OWF sites, once an initial ground model is established (usually on the basis of geophysics), ground investigations usually consist of a relatively limited number of boreholes (in comparison to the size of the site) complemented with a comparably large number of cone penetration tests, CPTs. It is good practice to have at least one CPTu at each WTG/monopile location. As such, although the calibration of the constitutive models is carried out on the basis of in-situ and laboratory tests from across the wind farm site, the application of the constitutive models in the 3D FE analysis of a particular monopile foundation is based primarily on the CPTu profile at that WTG location.

The deposits encountered in the large areas covered by OWF sites commonly consist of a variety of soils, including different types of sands, glacial tills, sedimentary clays, etc. “Complex” materials, including, for example, silts and other transitional soils, micaceous materials, laminated soils, chalk etc. can also be found. This paper focuses on sands of varying density and stiff clays of varying plasticity.

The paper is divided into two parts; the first part, which forms the majority of the paper, discusses the application of constitutive models in simulating the response of sands of varying density. It presents the calibration of two elasto-plastic constitutive models to the in-situ and laboratory test data of a sand dominated wind farm, highlighting the associated challenges. The models adopted are i) a strain softening Mohr-Coulomb model (Potts et al., 1990; Potts and Zdravkovic, 1999), which has previously been adopted in the design of monopile foundations for OWFs (Grammatikopoulou et al., 2007, 2020; Schroeder et al., 2020) and ii) a state parameter-dependent constitutive model based on the Mohr-Coulomb failure criterion (Taborda et al., 2018). Both models are combined with the Imperial College Generalised Small Strain Stiffness elastic model (IC.G3S, Taborda et al., 2016) also previously applied in offshore monopile foundation design (Grammatikopoulou et al., 2020). The ability of the models to reproduce the measured soil response is demonstrated through comparisons of single element simulations and laboratory test results. The calibration of the state-parameter dependent model highlights the difficulties encountered in establishing the critical state line on the basis of laboratory test data, emphasising the complexity of interpreting sand behaviour in a consistent manner. As such, two calibrations of this model, which make different assumptions with regard to the critical state line, are presented. The performance of the strain softening Mohr-Coulomb model and the two different calibrations of the state parameter-dependent model are then compared in the 3D FE analysis of an example monopile foundation from a sand-dominated offshore wind farm. In addition, a small study on the effect of the parameter choices in the strain softening Mohr-Coulomb model on the predicted monopile response is also presented.

The second part of the paper examines the use of constitutive models to simulate the behaviour of stiff clays with varying plasticity. The enhanced version of the Modified Cam Clay model adopted in the PISA work for the Cowden till (Zdravkovic et al., 2020b) is shown to reproduce successfully the response of the low plasticity glacial till deposits, whilst high plasticity clay deposits prove more difficult to model and different options are discussed.

Although the paper discusses the application of the constitutive models in the analysis of monopile foundations, the findings related to the calibration of the constitutive models and their ability to simulate the soils’ response at an element level are not limited to the geotechnical problem chosen to be analysed.

All the analyses presented in this work have been carried out using the FE code ICFEP.

2 MODELLING SANDS

2.1 Constitutive models

Modelling the behaviour of sand deposits can be complex, as their response has been shown to depend on both stress state and density, and a number of sophisticated constitutive models have been developed to simulate their behaviour (e.g. Dafalias and Manzari, 2004; Jefferies, 1993; Papadimitriou and Bouckovalas, 2002; Pestana and Whittle, 1999; Taborda et al., 2014). The majority of these models are based on the state parameter concept proposed by Been and Jefferies (1985), shown schematically in Figure 1. The state parameter, ψ, defined as the difference between the current void ratio, e, and that at critical state, e_{cs}, for the same mean effective stress, p', has been shown to explain the effect of both stress level and density on the response of sands.

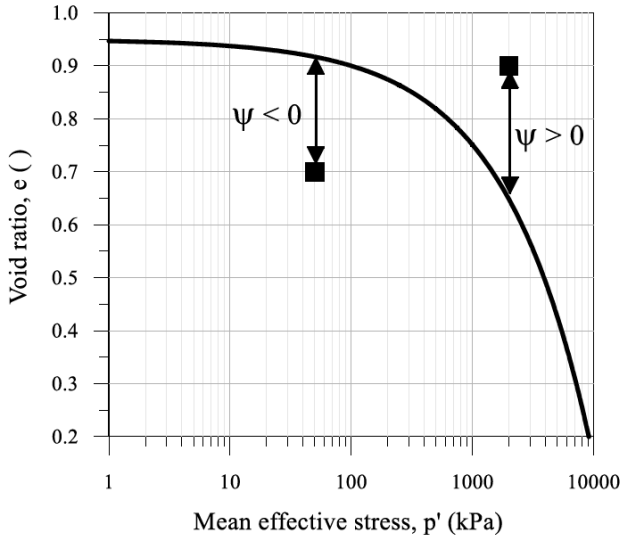

Figure 1. Definition of state parameter concept according to Been and Jefferies (1985)

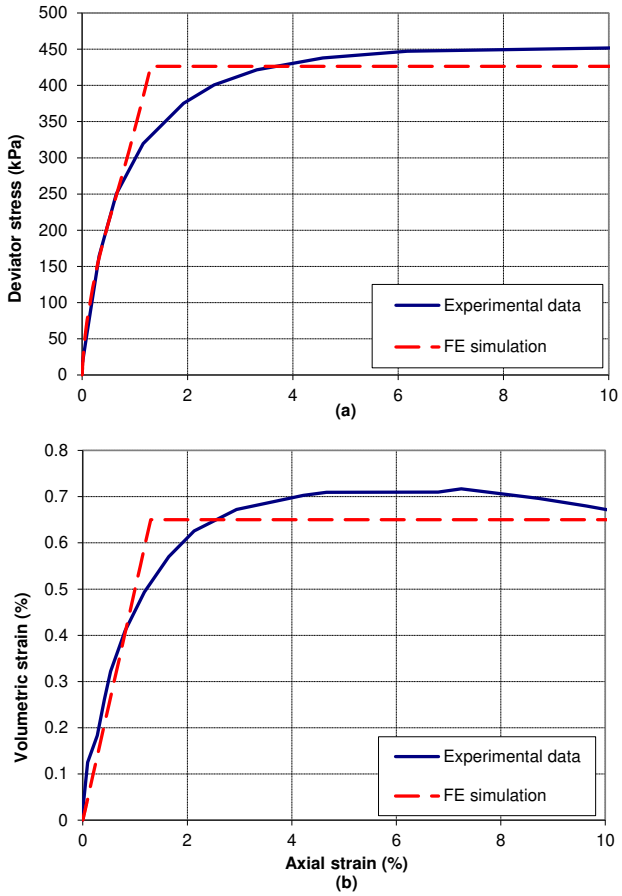

Figure 2. Comparison of experimental data and model predictions of simple Mohr-Coulomb model for looser-than-critical sand a) stress-strain response b) volumetric response (from Grammatikopoulou et al., 2017)

However, in practice such models are not often used. Instead, simpler models which make use of the Mohr-Coulomb failure criterion, are commonly adopted. An example is a simple elasto-plastic model in which the Mohr-Coulomb failure criterion is used as a yield surface and a non-associated flow rule with a constant angle of dilation is adopted (Potts and Zdravkovic, 1999). This type of model can, at least qualitatively, simulate the contractive response of sands that are looser than critical, if the angle of dilation is assumed to be equal to zero. An example can be seen in Figure 2 which compares an isotopically consolidated drained (CID) triaxial compression test on a looser than critical sand specimen with a single element FE simulation using such model. However, the same constitutive model cannot reproduce the response of denser than critical sands, as can be seen in Figure 3, as it neither captures the softening from peak to critical state nor the volumetric response. In this figure FE simulations with a zero angle of dilation and a non-zero constant angle of dilation are shown. It can be seen that, as expected, the former does not predict any dilative response, whilst the latter results in the prediction of unlimited dilative strains, neither of which agree with the measured response.

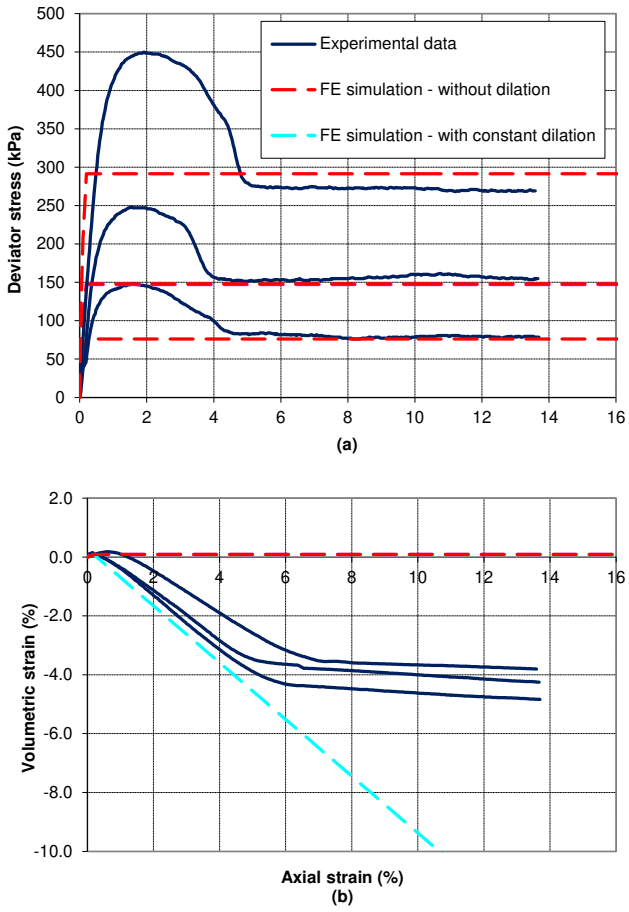

Figure 3. Comparison of experimental data and model predictions of simple Mohr-Coulomb model for denser-than-critical sand a) stress-strain response b) volumetric response (from Grammatikopoulou et al., 2017)

2.1.1 Strain-softening Mohr-Coulomb model

An improvement to the simple elasto-plastic model set out above is a strain-softening variation of the Mohr-Coulomb model, in which the angle of shearing resistance, cohesion and dilation are allowed to vary with plastic deviatoric strains, E_d (Potts et al., 1990; Potts and Zdravkovic 1999). This model, which has been adopted in the work presented in this paper, has previously been

used by the authors in the design of monopiles for OWFs in the North Sea and has been shown to reproduce well the response of the marine sands encountered at those sites, when coupled with appropriate non-linear elastic models (Grammatikopoulou at al., 2020; Schroeder et al., 2020). As an example, Figure 4 compares the results of a CID triaxial test on a dense marine sand with the simulations using this model, when the angle of shearing resistance is assumed to vary from peak to critical state, as shown in Figure 5(a), and in a similar manner the dilation is allowed to vary from the peak value to zero, as shown in Figure 5(b) (in this simulation the cohesion is assumed to be zero throughout). Figure 4 shows that this type of model can simulate the drop of strength from peak to critical state and the corresponding volumetric response. The input parameters for this model are the strength parameters related to the Mohr-Coulomb failure criterion, i.e. cohesion, c', and angle of shearing resistance, φ', the angle of dilation, ν, and the variation of these parameters with plastic deviatoric strain.

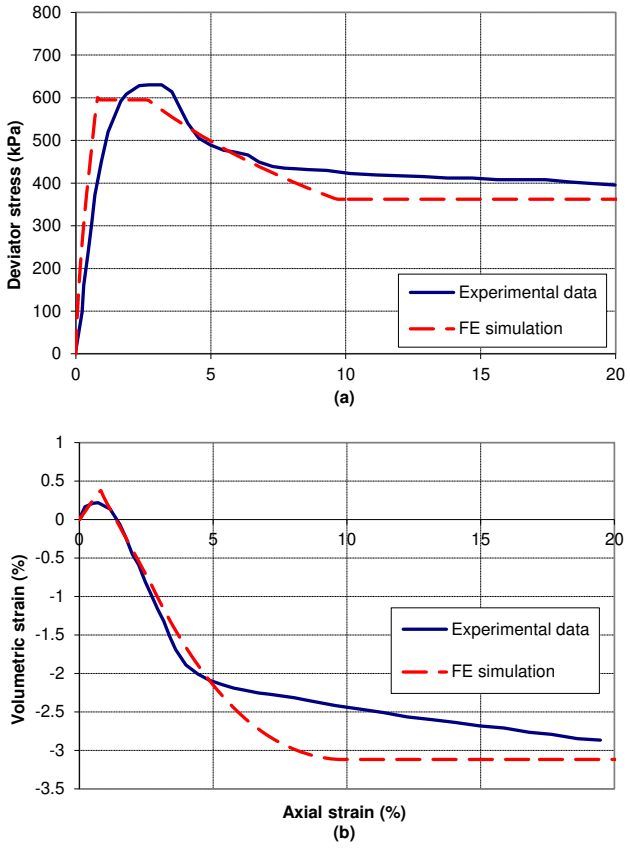

Figure 4. Comparison of experimental data and model predictions of strain-softening Mohr-Coulomb model for denser-than-critical sand a) stress-strain response b) volumetric response (from Grammatikopoulou et al., 2017)

Whilst this strain-softening variation of the Mohr-Coulomb model has been adopted with success in modelling the response of sand, the use of this model, and generally any Mohr-Coulomb based constitutive models of this type, comes with limitations; the input parameters need to be selected on the basis of the density and stress level of the sands encountered in the field. As such, different input parameters are likely to be needed to represent varying densities and stress states of sands in any particular boundary value problem. In addition, as the peak strength and dilatancy are input parameters in this model, they will remain constant during any given analysis. Consequently, the influence of any changes in stress level and density during the analysis will not be captured.

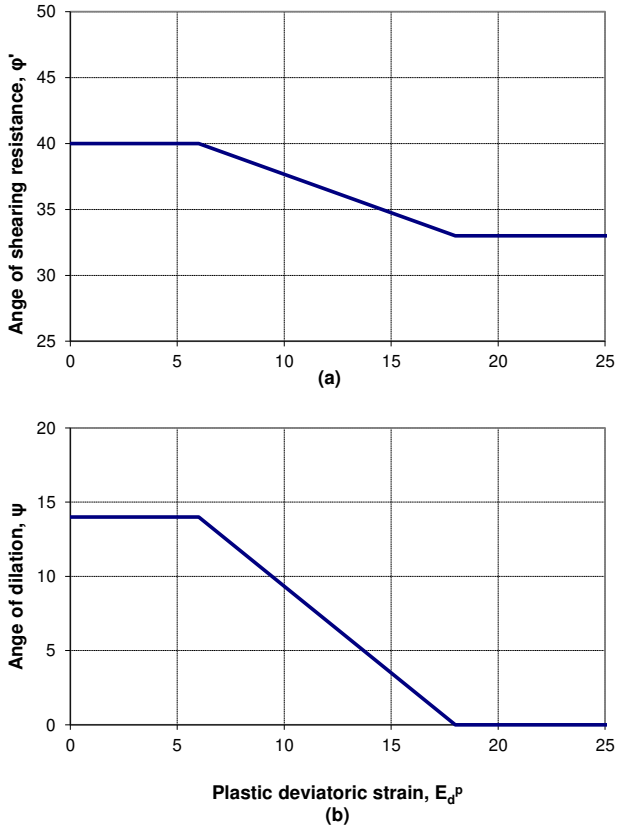

Figure 5. Variation of angle of a) shearing resistance and b) dilation with plastic deviatoric strain assumed for a dense sand assumed in strain-softening Mohr-Coulomb model (from Grammatikopoulou et al., 2017)

2.1.2 State parameter-dependent model

The second elasto-plastic constitutive model adopted in this work is the state parameter-dependent constitutive model proposed by Taborda et al. (2018). In this model the Mohr-Coulomb failure criterion is enhanced by introducing a direct link with the state parameter concept. In this way the model can take account of the effect of the state parameter on the material's strength and dilatancy, whilst retaining the simplicity of the Mohr-Coulomb failure criterion. Some basic equations of the model are given below. For further details the reader is referred to Taborda et al. (2018).

The Critical State Line (CSL) is described by a power law (after Li and Wang, 1998):

$$e_{CS} = e_{CS,ref} - \lambda \cdot \left(\frac{p'}{p'_{ref}}\right)^{\xi} \qquad (1)$$

where p'_{ref} is a reference pressure and $e_{cs,ref}$, λ and ξ are input parameters.

The model assumes a Mohr-Coulomb failure criterion as the yield surface, coupled with a non-associated flow rule, where both the current angle of shearing resistance, φ_c, and the current angle of dilation ν_c, are dependent on the state parameter, ψ. Figure 6 shows a schematic representation of the yield and plastic potential surfaces in the *q-p´* plane adopted by the model for a purely frictional material.

The gain in available strength, M_s, is related to the state parameter, ψ, through the model parameter, k, as follows:

$$M_S = M_{CS} + k\langle -\psi \rangle \quad (2)$$

where M_{CS} is the stress ratio (q/p') at Critical State for triaxial loading conditions and $\langle \ \ \rangle$ are the Macauley brackets, according to which $\langle A \rangle = A$ if $A > 0$ and $\langle A \rangle = 0$ if $A \leq 0$. The current angle of shearing resistance, φ_c, is calculated as:

$$\varphi_c = arcsin\left(\frac{3 \cdot M_S}{6 + M_S}\right) \quad (3)$$

The stress ratio defining the inclination of the plastic potential, M_D, is related to the state parameter, ψ, through the model parameter, l, as follows:

$$M_D = l\langle -\psi \rangle \quad (4)$$

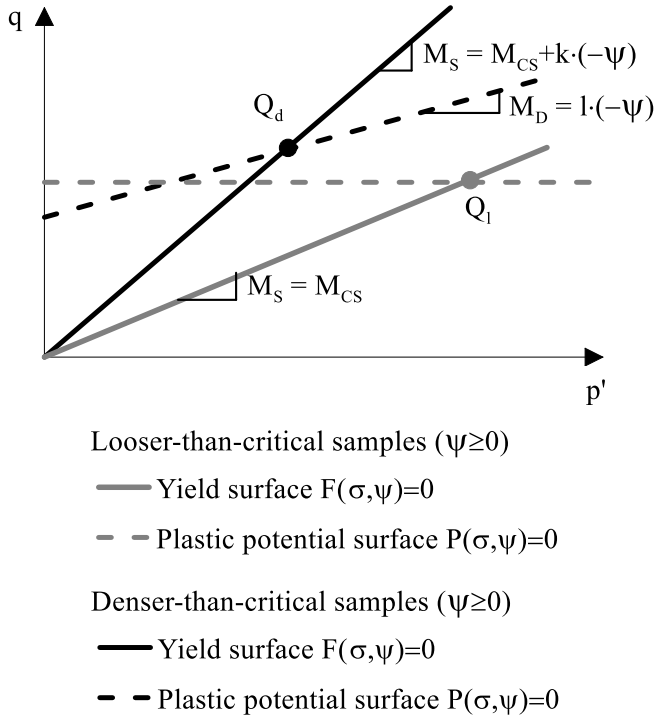

Figure 6. Yield and plastic potential surfaces adopted by the state parameter-dependent model for a purely frictional material (from Taborda et al. 2018)

The current angle of dilation, ν_c, is calculated as:

$$\nu_c = \arcsin\left(\frac{3 \cdot M_D}{6 + M_D}\right) \quad (5)$$

As a consequence of Equation (2), for looser-than-critical samples (i.e. $\psi > 0$), the strength of the material is limited to that corresponding to the Critical State. For denser-than-critical samples (i.e. $\psi < 0$), the available strength is controlled by Equation (2).

It is noted that in this model the concept of the "plastic" state parameter is introduced, with the state parameter in Equations (2) and (4) being given on the basis of the following approximation:

$$\psi \approx \psi^p = e^p - e_{CS} \quad (6)$$

where e^p is the "plastic" void ratio. For further details see Taborda et al. (2018).

The model has three parameters related to the CSL, $e_{cs,ref}$, λ and ξ (in addition to the reference pressure, p'_{ref}), two parameters related to the Mohr-Coulomb failure criterion, c', and φ'_{cs}, and two parameters that describe the effect of the state parameter on the strength and dilatancy of the material, k and l. This model has the advantage of being able to simulate the response of sands at different densities and stress states with a single set of parameters, taking account of any changes to density and stress state during the analysis. Moreover, it has a relatively small number of parameters, as compared to other constitutive models based on the state parameter concept, making its use attractive.

This state parameter-dependent model has recently been used by the authors in combination with the IC.G3S model, discussed below, in the design of monopiles; this forms the basis of the work presented herein.

2.1.3 IC.G3S non-linear elastic model

The constitutive models employed in the analyses of monopile foundations need to be able to reproduce the soil response throughout the whole strain range, from very small to large strains as this will affect the predicted movements and rotations and hence the predicted performance of these structures at serviceability limit states, as well as the failure mechanism in the ultimate limit state. When the PISA methodology is adopted in monopile design, this will also affect the soil reaction curves extracted from the 3D FE analyses, which in turn will affect the results obtained from the 1D beam models used in design. As such, it is important to model the non-linear response of the soil and the degradation of stiffness with strain.

In the current work the strain-softening Mohr-Coulomb model and the state parameter-dependent model were combined with the IC.G3S non-linear elastic model (Taborda et al. 2016). This model allows the simulation of a variety of features, including non-linearity

from early stages of loading, as well as dependence of stiffness on stress state and void ratio, which are particularly important for the modelling of sands.

In the IC.G3S model the maximum shear modulus, G_0, at very small strains is given by the following equation (Taborda et al. 2016):

$$G_0 = G_{ref} \cdot f_G(e) \left(\frac{p'}{p'_{ref}}\right)^{m_G} \quad (7)$$

where G_{ref} is a reference shear stiffness, p'_{ref} is a reference pressure, m_G is a parameter defining the dependence of G_0 on p', and $f_G(e)$ is a function which incorporates the influence of void ratio. Taborda et. al (2016) list a number of formulas that can be adopted in the IC.G3S model for $f_G(e)$. In the current work the following function was used (Lo Presti et al, 1993):

$$f_G(e) = e^{-f_{e,G}} \quad (8)$$

where $f_{e,G}$ is an additional parameter.

The IC.G3S model uses a modified hyperbolic function to describe the degradation of soil stiffness with strain, with the dependence of the tangent shear stiffness, G_{tan}, on E_d, the generalised deviatoric strain, given by the following equation:

$$G_{tan} = G_0 \cdot \left(R_{G,min} + \frac{1-R_{G,min}}{1+\left(\frac{E_d}{a}\right)^b} \right) \quad (9)$$

where G_0 is given by Equation (7) and a, b and $R_{G,min}$ are model parameters. In the work presented herein the variation of shear stiffness with strain given in the above equation was combined with a constant Poisson's ratio, μ.

2.2 *Calibration of constitutive models*

2.2.1 *Sand deposits at offshore wind farm site*

The predominant soils encountered at the OWF site considered in this work are two sand deposits, termed here Sand A and Sand B. Sand A is generally encountered at shallow depths, whilst Sand B is generally encountered at deeper depths across the wind farm site. A high quality ground investigation of the OWF was undertaken comprising in situ and laboratory testing. In addition to general characterisation tests, the laboratory investigation included a comprehensive triaxial testing programme for each sand deposit with isotropically consolidated drained tests (CID) carried out at different densities and confining pressures. A number of advanced triaxial tests were also carried out, which included local instrumentation and bender element testing. The confining pressures and relative densities chosen for the triaxial tests reflected the range of depths encountered across the OWF site and the range of relative densities interpreted from the available CPTs. The relative density, D_r, of the samples tested varied between approximately 40% and 100% for Sand A and 45% and 95% for Sand B. Resonant column tests on samples of the two sands were also undertaken. The majority of the tests on each sand were carried out on samples originating from a batch for each sand formed from samples taken from across the wind farm site with similar granulometry and mineralogy. These batches are termed here Batch 1 and Batch 2 for Sand A and Sand B, respectively. In addition, some tests were carried out on individual samples from boreholes at specific monopile locations.

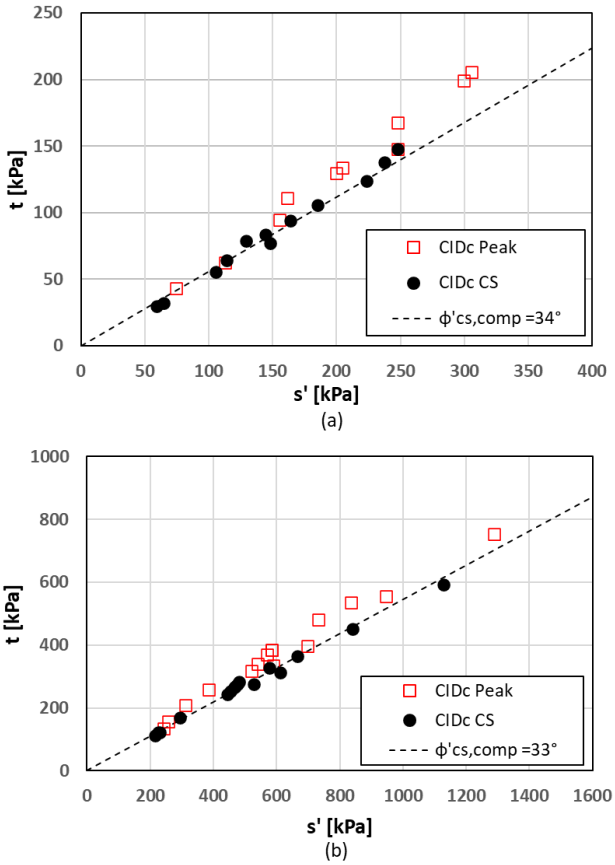

Figure 7. Peak and critical state stress states a) Sand A b) Sand B

There are two input parameters that are common between the two constitutive models, i.e. the strength parameters at critical state, c', and φ'_{cs}. Figure 7 shows the peak and critical state stress states established on the basis of the CID tests on the two sands. As expected, the peak stress states are variable as they depend on the density and stress state of the samples tested. However, the critical state stress states are more consistent and indicate angles of shearing resistance, φ'_{cs}, equal to 34º and 33º, together with $c' = 0$ for Sand A and B, respectively. As the remaining input parameters are different for the two models, the calibration of each model is presented

separately in the following two sections, with the calibration of the state parameter-dependent model being presented first.

2.2.2 State parameter-dependent model

In order to establish the CSL in e-log(p') space, the results of the CID tests are plotted for the batch samples of each sand in Figure 8, together with the estimated critical states of these tests, calculated on the basis of the final global void ratio measured at the end of the tests. The approximate relative density of the samples are also indicated in the same figure. Inspection of Figure 8 shows that, as expected, the dense samples dilate more than the medium dense and loose samples, at similar confining pressures. However, the estimated critical states of the CID tests do not fall on a unique line, which makes the derivation of the position of the CSL in e-log(p') space challenging.

According to Jefferies and Been (2006) the location of the CSL should ideally be established on the basis of very loose samples (with D_r <30%) consolidated to reasonably high effective stresses, to ensure that the samples are looser than critical (i.e. $\psi > 0$) and exhibit compressive volumetric strains during shearing. This is because samples that are denser than critical (i.e. $\psi < 0$) tend to dilate and the interpretation of the tests becomes complicated due to strain localisation and the formation of shear banding in later stages of the triaxial tests. It is noted that the samples tested were sheared to axial strains of 20%, which is significantly higher than in standard commercial tests. Nonetheless, Figure 8 shows that the estimated critical state points of the dense samples lie considerably lower than the ones for the loose samples, highlighting the complexity of defining a unique CSL, on the basis of triaxial test results.

The problem of strain localisation and shear banding in triaxial testing of dense sand samples and the difficulties in the interpretation of these tests is well known and discussed by many researchers (e.g. Chu, 1995; Desrues et al., 1996; Jefferies and Been, 2006; among others). As an example, the computed tomography work by Desrues et al. (1996) suggests that the global measurements of void ratio in dense dilating sand samples may not be physically relevant. Instead, in their work the measurements of void ratio developing within the shear zones themselves indicated a limit value which agrees with the one established on the basis of loose samples and is independent of the initial density of the sample. However, this was based on a limited number of tests carried out at the same confining pressure. Clearly, this is an area where further research is required.

The challenges in identifying a unique position of the CSL of Dunkirk Sand have also been discussed in the work of Zdravkovic et al. (2020a) and Taborda et al. (2020) who found different CSL positions on the basis of CID tests carried out on samples at a range of confining pressures with two different relative densities ($D_r \approx$ 45% and $D_r \approx$ 75%).

As indicated in Figure 8, in the current case there is only one test with a low relative density (in the order of 40-45%) for each sand and it is clear that the tests with higher densities do not reach the CSL defined on the basis of these relatively loose samples (indicated with the solid lines in Figure 8). Figure 8 also shows that the higher the density of the samples, the lower the estimated critical states plot in the e-log(p') space.

Therefore, the constitutive modeller has to decide whether to choose a unique CSL on the basis of the relative loose samples, or, perhaps, to use a CSL which agrees with the end points of relevant tests, despite the limitations in the interpretation of these tests. In the latter case different CSL positions may be defined for different relative densities as indicated in Figure 8, with the different broken lines.

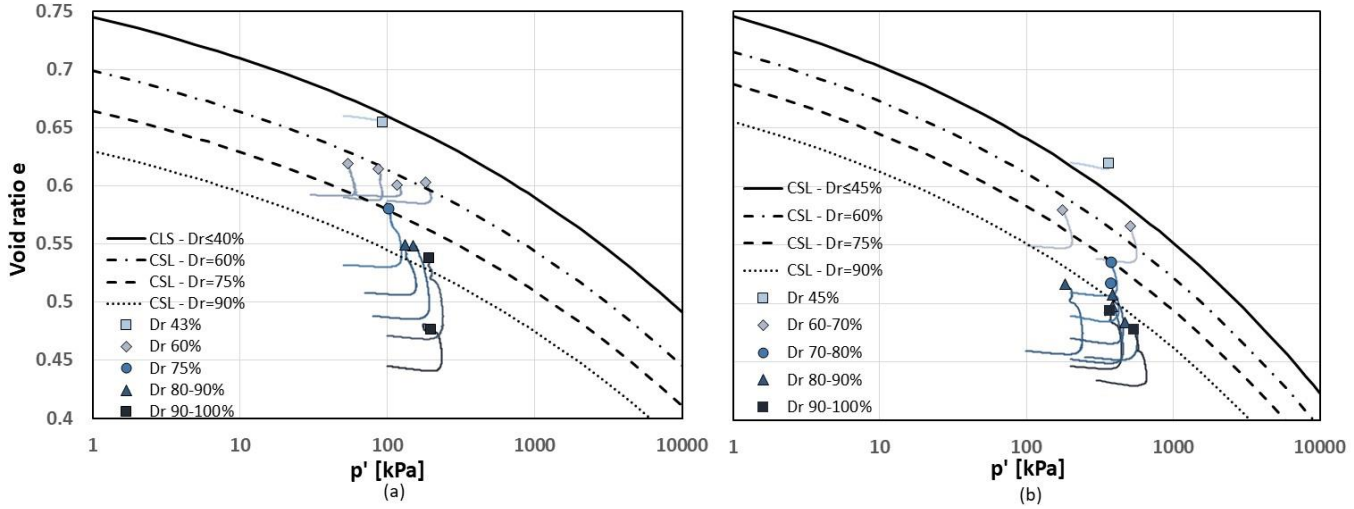

Figure 8. Critical state line in e-log(p') space and results of CID tests on batch samples a) Sand A b) Sand B

It is noted that for the first option, in any state parameter-based constitutive model, the denser than critical samples would dilate to the unique CSL defined on the basis of the looser samples, i.e. the paths would be assumed to dilate significantly more than indicated by the tests. In the current work both options were explored and two calibrations of the state parameter-dependent model were carried out. In the first calibration (Calibration 1) a unique position of the CSL was assumed on the basis of the relatively loose samples, whilst in the second calibration (Calibration 2) the position of the CSL was assumed to depend on relative density. As discussed in detail below, Calibration 1 results in significantly higher dilative strains than measured in the CID tests. On the other hand, Calibration 2 is a practical way of reproducing the dilative response measured in the CID tests but does not agree with the theoretical framework of critical state soil mechanics. It is noted that the different positions of the CSL in Figure 8 are achieved by varying the parameter $e_{CS,ref}$ in the expression for the CSL (Equation (1)), whilst keeping the remaining parameters λ, ξ and p'_{ref} constant.

Figure 9 presents the data plotted in Figure 8 together with the results from CID tests on non-batched samples of Sand A and Sand B taken from specific monopile locations. This figure shows that for Sand A the test with D_r = 90% compares well with similar tests on Batch 1 samples. However, for Sand B there are some non-batch tests which do not agree with the batch tests. A detailed review shows that, in particular samples S1 and S5, have significantly different e_{min} and e_{max} values to those for Batch 2 (see Figure 10). This results in different initial void ratios, e_0, for a given relative density, a different position in the e-log(p') space, and consequently an inconsistency with the position of the CSL defined on the basis of the batch samples. As such, samples with significantly different e_{min} and e_{max} values cannot be used in the derivation of the CSL and hence in the calibration of state parameter-dependent constitutive models. This poses significant challenges for naturally variable materials and suggests that the use of batch samples may be one way of addressing this variability.

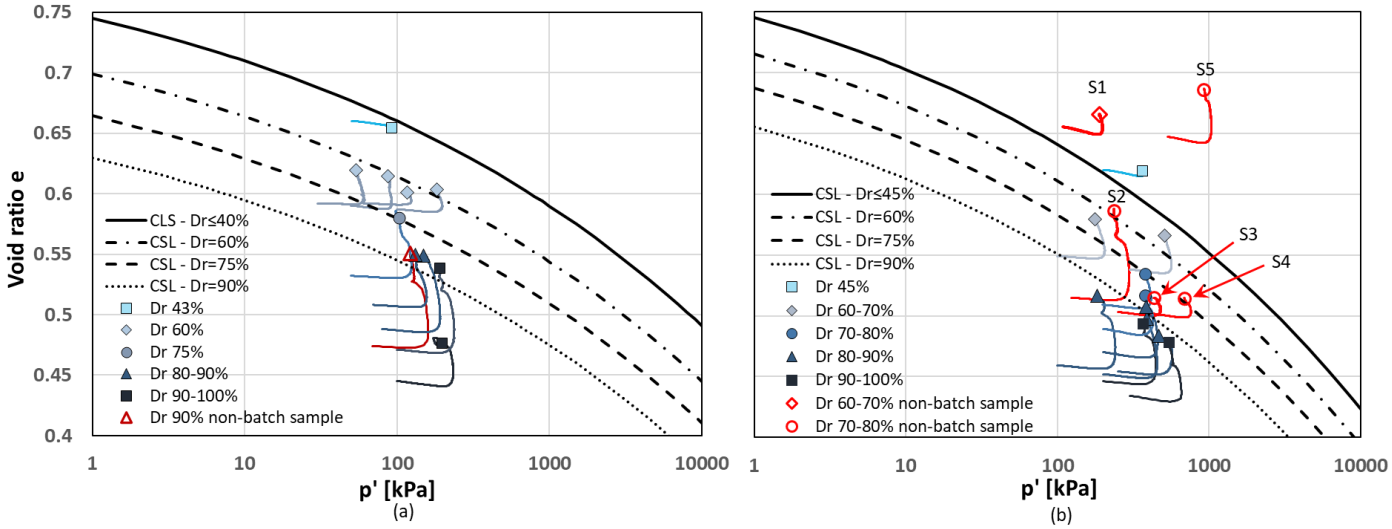

Figure 9. Critical state line in e-logp´space and results of CID tests on batch and non-batch samples a) Sand A b) Sand B

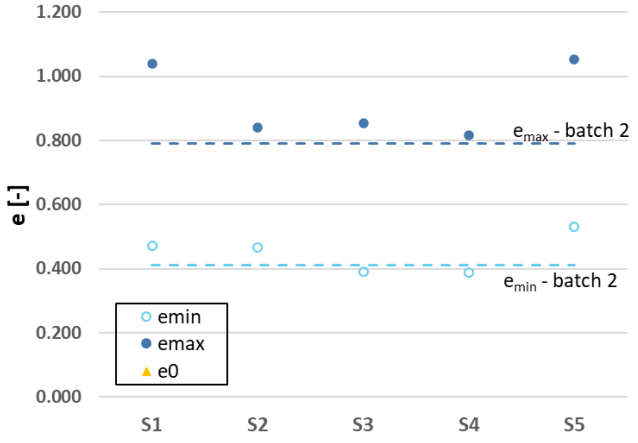

Figure 10. Minimum, maximum and initial void ratio (at the start of shearing) of non-batch samples of Sand B

The remaining two parameters of the model are k and l which describe the effect of the state parameter on the strength and dilatancy of the material (Equations (2) and (4)). The calibration of these parameters is demonstrated here for one of the sand deposits, Sand B. The same procedures were adopted for the calibration of these parameters for Sand A.

In order to calibrate the parameter k which controls the strength of the material, the mobilised stress ratio in the CID tests is plotted against the current state parameter (Taborda et al. 2018). This is shown in Figure 11 for the two calibrations, i.e. Calibration 1, with a unique CSL and Calibration 2, with a density-dependent CSL. The mobilised stress ratio is the same in Figure 11(a) and Figure 11(b) but the state parameter, ψ, is different, as it is calculated in relation to the assumed CSL.

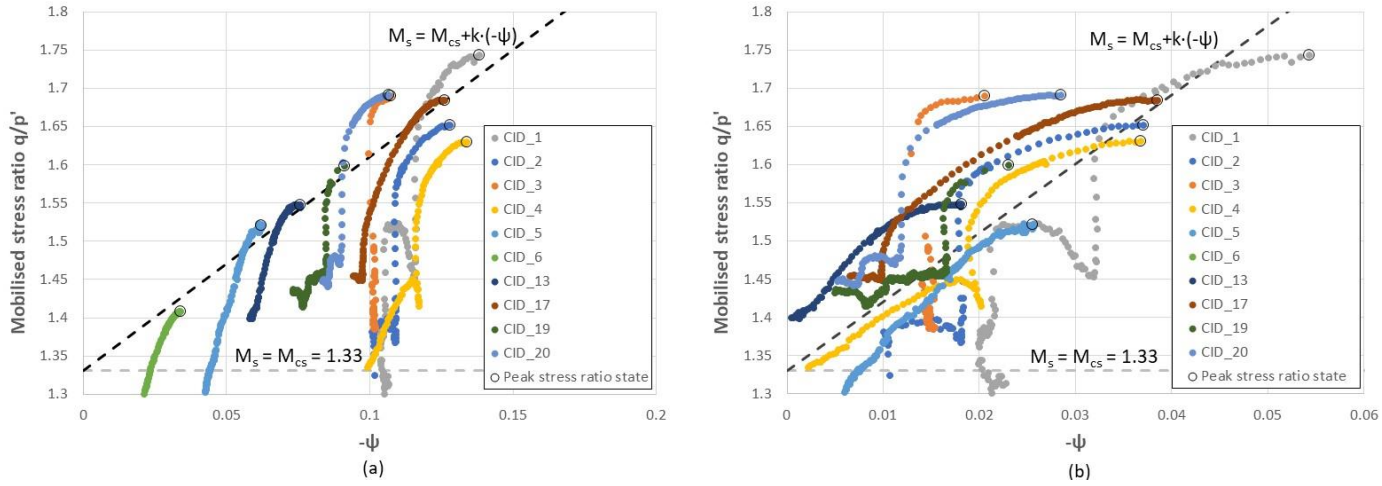

Figure 11. Calibration of parameter k in state parameter-dependent model for Sand B a) Calibration 1 b) Calibration 2

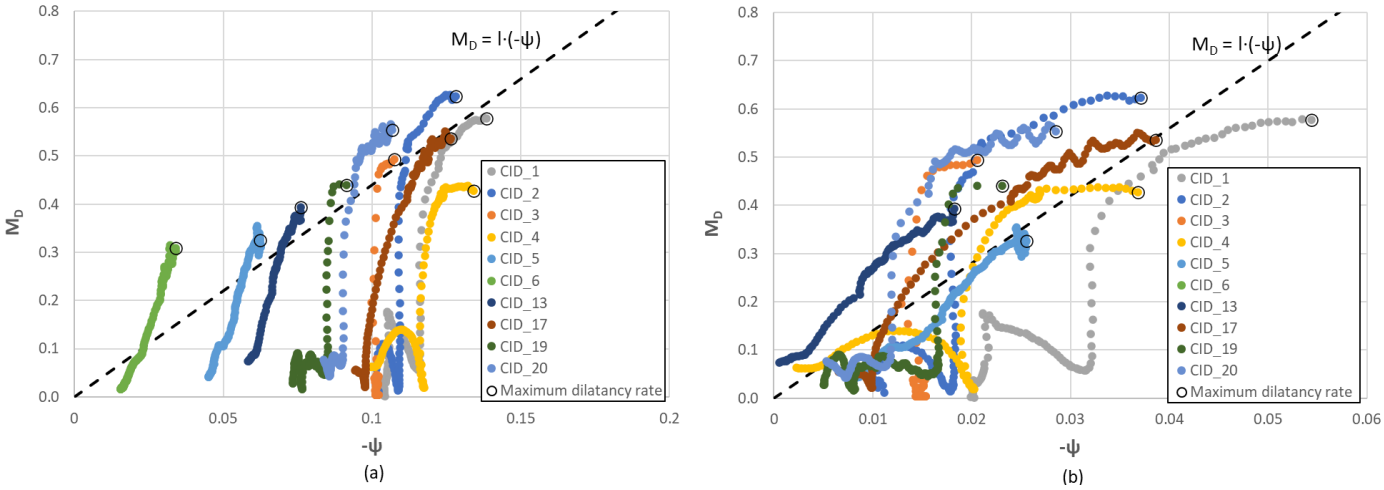

Figure 12. Calibration of parameter l in state parameter-dependent model for Sand B a) Calibration 1 b) Calibration 2

It is noted that only the post-peak portion of the tests are presented in Figure 11 (with the maximum stress ratio of each test marked), as this is the part simulated by the state parameter-dependent constitutive model; the pre-peak behaviour is governed by the IC.G3S non-linear elastic model. Moreover, the state parameter ψ is plotted instead of ψ^p (adopted in Equation (6)), as suggested in Taborda et al. (2018), based on the fact that elastic strains tend to be much smaller than plastic strains. Figure 11 shows that for both calibrations the mobilised stress ratio reduces gradually with shearing, approaching the assumed strength at critical state M_{cs} = 1.33 (which corresponds to the assumed angle of shearing resistance φ'_{cs} = 33º for sand B seen in Figure 7). However, whilst for Calibration 2 the value of the state parameter generally approaches zero as the mobilised stress ratio reduces to critical state (see Figure 11(b)), this is not the case for Calibration 1 (see Figure 11(a)). This reflects the fact that the end points of the tests on the denser than critical samples do not reach the CSL used in Calibration 1, i.e. that defined on the basis of the looser samples.

For the calibration of the parameter *l*, a similar process is carried out in which the dilatancy rate, M_D, is plotted against the current state parameter, see Figure 12. As in Figure 11, Figure 12 plots the state parameter ψ instead of ψ^p. In addition, the total dilatancy rate is plotted, instead of the plastic dilatancy rate, for the reasons discussed above. It is noted that, similar to Figure 11, only the post-peak response is presented in Figure 12. In addition, the maximum dilatancy rate measured in each test is indicated on the graphs. Figure 12 shows that with increased shearing this quantity reduces gradually and approaches zero which would indicate critical state conditions (noting the discussions earlier on the limitations of the interpretation of these tests). However, similar to Figure 11, this coincides with the state parameter approaching zero in Calibration 2 but not in Calibration 1.

Tables 1 and 2 summarise the parameters of the state parameter-dependent model for Sand A and Sand B respectively.

Table 1. Summary of parameters of state parameter-dependent model for Sand A

Parameter	Calibration 1	Calibration 2
$e_{CS,ref}$	0.83	0.83-0.0023·(D_r-40)*
λ	0.17	0.17
ξ	0.15	0.15
p'_{ref} (kPa)	100.0	100.0
φ'_{cs} (°)	34	34
c' (kPa)	0.0	0.0
k	2.4	9.0
l	3.75	15.5

* D_r is expressed in %

Table 2. Summary of parameters of state parameter-dependent model for Sand B

Parameter	Calibration 1	Calibration 2
$e_{CS,ref}$	0.841	0.841-0.002·(D_r-45)*
λ	0.2	0.2
ξ	0.16	0.16
p'_{ref} (kPa)	100.0	100.0
φ'_{cs} (°)	33	33
c' (kPa)	0.0	0.0
k	2.8	9.0
l	4.4	14.0

* D_r is expressed in %

2.2.3 *Strain softening Mohr-Coulomb model*

As discussed in Section 2.1.1, the input parameters for the strain-softening Mohr-Coulomb model are the cohesion, c', the angle of shearing resistance, φ', the angle of dilation, v, and the variation of these parameters with the deviatoric plastic strain. Since in this study the non-linear elastic model IC.3GS is used to model the pre-peak response of the sands, it is necessary to define the variation of these parameters from peak to critical state conditions.

In the current work, the input parameters were varied on the basis of relative density. Two variations were assumed: one corresponding to dense states, i.e. $D_r \approx$ 60-80% and one to very dense states, i.e. $D_r \approx$ 80-100%[1]. Figure 13 replots the data from Figure 7 differentiating the CID tests' peak stress states in terms of dense and very dense states. Also shown in these graphs are peak angles of shearing resistance, φ'_{peak}, for the two different density ranges, as well as the critical state angles of shearing resistance, φ'_{cs}, which are independent of the sand density, and as previously discussed, were assumed to be equal to 34° and 33°, for Sand A and B, respectively. Figure 14 presents the assumed variations of the angle of shearing resistance for the two sand deposits, in which φ' is shown to vary from the peak values, φ'_{peak}, defined in Figure 13 to the critical state values, φ'_{cs}.

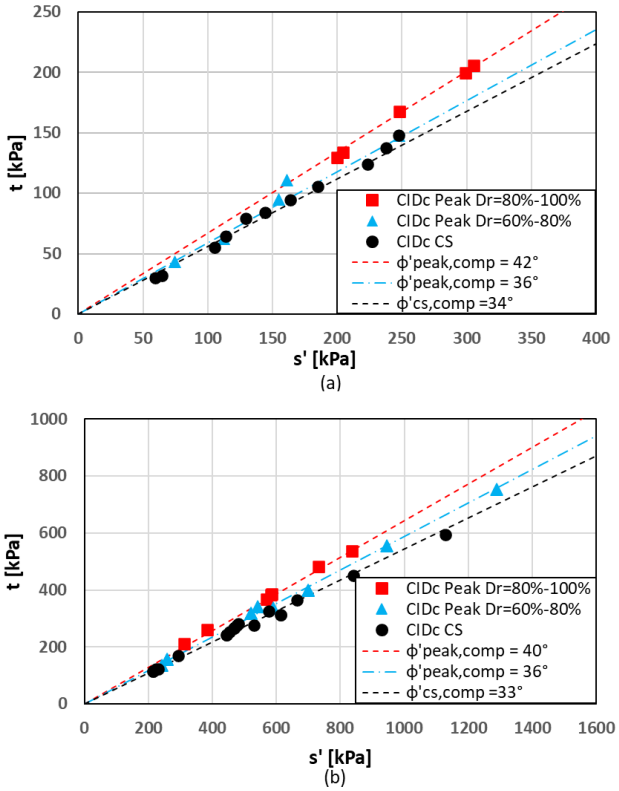

Figure 13. Peak angles of shearing resistance for different relative densities a) Sand A b) Sand B

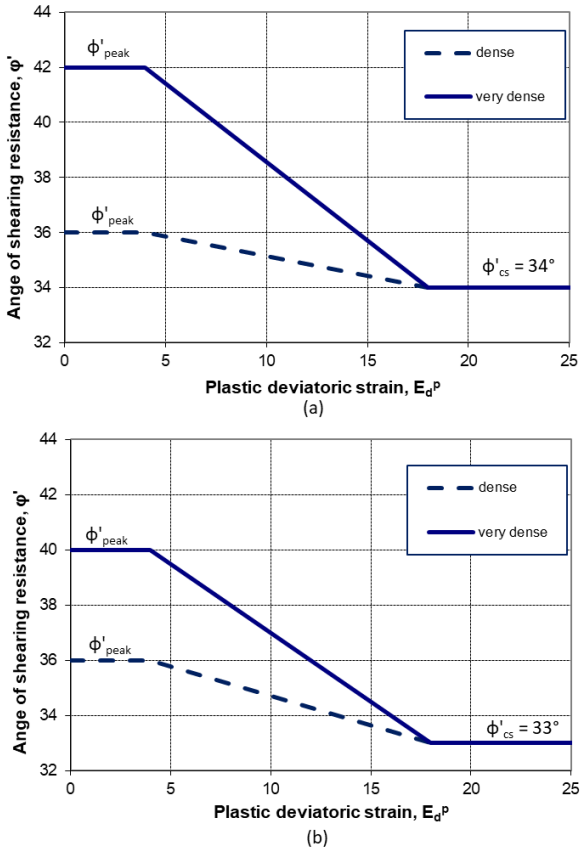

Figure 14. Variation of angle of shearing resistance assumed in strain-softening Mohr-Coulomb model a) Sand A b) Sand B.

[1] It is noted that the classification adopted for the dense and very dense states (i.e. $D_r \approx$ 60-80% and $D_r \approx$ 80-100%) is slightly different to the one used in the BS EN ISO 14688-2 and EC7-2 standards (i.e. $D_r \approx$ 65-85% and $D_r \approx$ 85-100%).

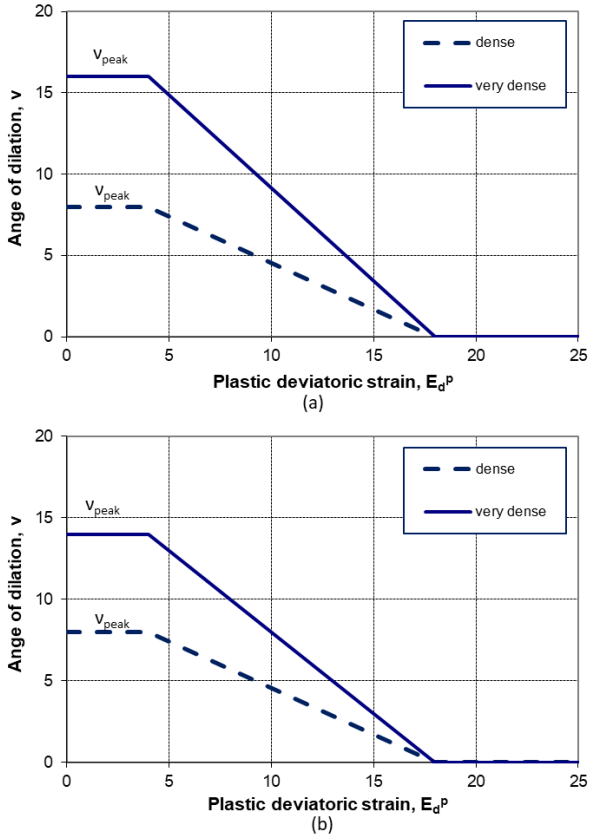

Figure 15. Variation of dilation assumed in strain-softening Mohr-Coulomb model a) Sand A b) Sand B

The angle of dilation, v, was also assumed to vary from the peak values, v_{peak}, to zero at critical state, in the manner shown in Figure 15. The v_{peak} values were based on the maximum dilatancy rate measured in the CID tests for the different relative densities.

For D_r < 60%, a constant angle of shearing resistance, $\varphi' = \varphi'_{cs}$, was assumed in combination with a constant angle of dilation equal to zero, i.e. as per Figure 2. It is noted that, for the example monopile location considered in the FE analyses (see Section 2.3 below), Sand A is encountered predominantly at dense to very dense states, i.e. $D_r \approx$ 60-95%, whilst Sand B is encountered at predominantly very dense states, i.e. $D_r \approx$ 80-100%.

Tables 3 and 4 summarise the peak and critical state angles of shearing resistance and dilation adopted for sand A and Sand B respectively. It is noted that the cohesion, c', was assumed to be zero for both sand deposits.

Table 3. Summary of peak and critical state angles of shearing resistance and dilation for Sand A

Density range	φ'_{peak} (°)	φ'_{cs} (°)	v'_{peak} (°)	v_{cs} (°)
<60%	34.0	34.0	0	0
60%-80%	36.0	34.0	8	0
>80%	42.0	34.0	16	0

Table 4. Summary of peak and critical state angles of shearing resistance and dilation for Sand B

Density range	φ'_{peak} (°)	φ'_{cs} (°)	v'_{peak} (°)	v_{cs} (°)
<60%	33.0	33.0	0	0
60%-80%	36.0	33.0	8	0
>80%	40.0	33.0	14	0

2.2.4 IC.G3S non-linear elastic model

It is generally accepted that the stiffness at very small strains, G_0, depends on the mean effective stress, p', to the power of n, where n = 0.5 is reasonably representative for sands. With the IC.G3S model this can be achieved by setting the parameter m_G in Equation (7) equal to 0.5. The remaining parameters of the IC.3GS model which control G_0, i.e. G_{ref}, p'_{ref} and $f_{e,G}$ were chosen for each sand deposit to reproduce, as closely as possible, the Rix and Stokoe (1992) G_0 interpretation of CPT profiles across the OWF area. In addition, a reasonable match was sought with G_0 measurements obtained from bender element (BE) and resonant column (RC) tests. This is further explained below, in Section 2.3, for the example monopile location considered in the FE analyses.

Figure 16(a) presents in-situ relative density profiles obtained from the CPT trace at the example monopile location by applying the relationships proposed by Baldi et al. (1986) and Jamiolkowski et al. (2003). It is noted that, on the basis of these CPT correlations, relative densities of more than 100% can be calculated. However, in the assessments presented in **Error! Reference source not found.**), the relative density has been capped at 100%. Figure 16(b) presents the G_0 profile obtained by applying the relationship proposed by Rix and Stokoe (1992) to the same CPT data. It is noted that in this figure G_0 is normalized by the maximum value in the idealised profile.

In order to calibrate G_{ref}, p'_{ref} and $f_{e,G}$ the required initial void ratio profiles are determined using idealised D_r profiles (see Figure 16(a)) for the example location in combination with the values of e_{min} and e_{max} assumed for each sand deposit. Using appropriate G_{ref}, p'_{ref} and $f_{e,G}$ parameters in Equations (7) and (8) it is then possible to match the Rix and Stokoe (1992) derived G_0 profiles for CPT profiles across the OWF area. Figure 16(b) demonstrates this for the example location. It is noted that it is generally possible to use a single set of parameters for all locations across the OWF.

For the example location, the results of the BE and RC tests are shown in Figure 16(b) with full symbols (circles are used to denote the BE tests, and triangles the RC tests). When comparing a CPT derived G_0 profile with laboratory test data, it is important to ensure compatible relative densities and stress levels. In the case of the data for the example location shown in Figure 16(b) the bender element and resonant column samples were

tested at different/lower relative densities than those encountered in-situ, warranting an appropriate adjustment. In this case, the adjustment was made applying Equations (7) and (8) with the CPT derived parameters. Figure 16(b) shows a good comparison between the adjusted laboratory test data (denoted using empty symbols) and the idealised G_0 profile.

The parameters of the IC.G3S model which control the stiffness degradation with strain, i.e. a, b and $R_{G,min}$ in Equation (9), were estimated on the basis of the advanced CID tests with local instrumentation. Figure 17 shows the results of these tests in terms of the normalised vertical tangent Young's modulus E', plotted against axial strain. Also shown in this figure are the results of the BE and RC tests (the latter are plotted against shear strain). In this figure E' has been normalised with an assumed theoretical value of E'_0 at very small strains, calculated on the basis of G_0 obtained from Equation (7) using the initial stress state and density of each sample (and assuming a Poisson's ratio μ equal to 0.25). Also shown in Figure 17 is the FE idealisation obtained with the IC.3GS model using the chosen parameters a, b and $R_{G,min}$ in Equation (9) and a constant Poisson's ratio, μ, equal to 0.25.

Table 5 summarises the parameters of the IC.G3S model for the two sand deposits.

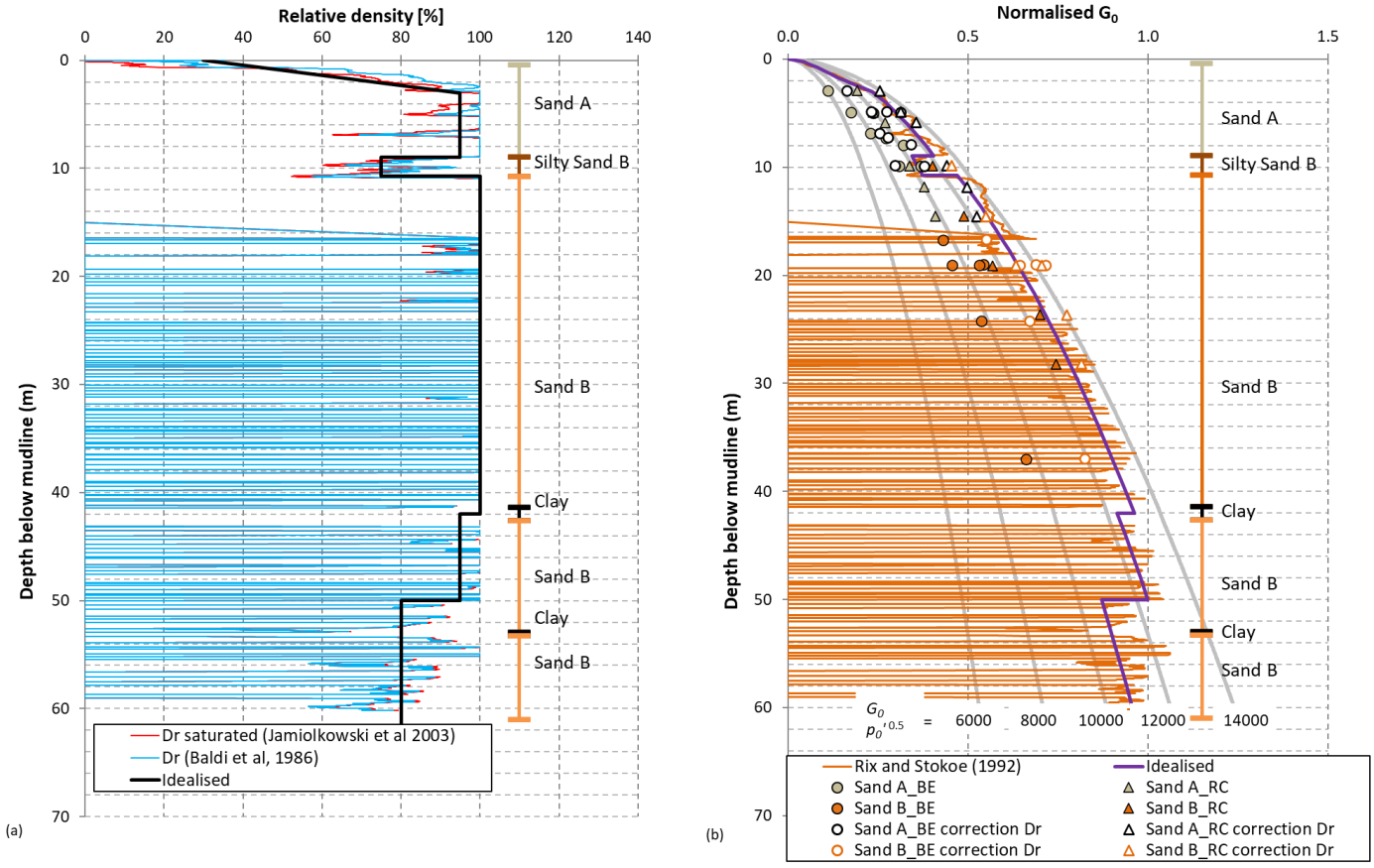

Figure 16. CPT interpretation and idealised response for sand deposits a) D_r and b) G_0

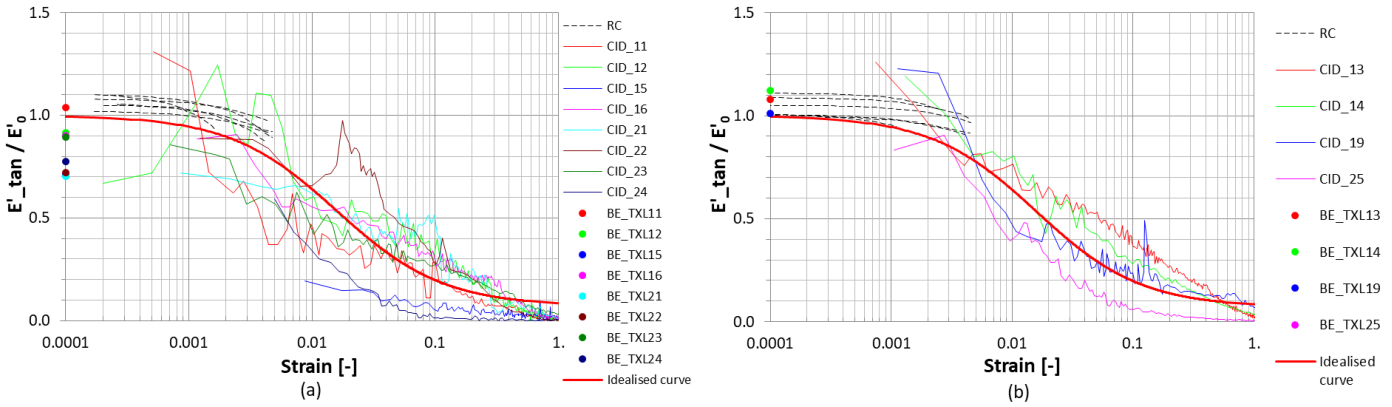

Figure 17. Stiffness strain response on the basis of CID tests, RC and BE tests and idealised response a) Sand A b) Sand B

Table 5. Summary of parameters of non-linear elastic IC.G3S model for Sands A and B

Parameter	Sand A	Sand B
G_{ref} (MPa)	52	49
p'_{ref} (kPa)	101.3	101.3
m_G	0.5	0.5
$f_{e,G}$	1.1	1.1
a	2.75x10^{-4}	2.75x10^{-4}
b	1.0	1.0
$R_{G,min}$	0.07	0.07
μ	0.25	0.25

2.2.5 Single element simulations

In order to assess the models' ability to reproduce the response of the two sand deposits at an element level, the CID tests were simulated in single element FE analyses using the FE code ICFEP and the predictions were compared with the results of the corresponding laboratory tests.

Figures 18 and 19 present simulations of two CID tests, using the state parameter-dependent model, for each of the two sand deposits, Sand A and Sand B respectively. The simulations are presented for Calibrations 1 and 2, discussed in Section **Error! Reference source not found.**. The CID tests that are reproduced in these figures have D_r > 80%, as these are the predominant relative densities encountered at the example monopile location. However, in order to provide insight into the model's capabilities of simulating the sands' response for varying stress states and densities with a single set of parameters, single element FE simulations of CID tests carried out at different relative densities, D_r, and confining pressures, p'_o, were also undertaken and are shown in Appendix A.

Figure 18 compares the model predictions and laboratory measurements for sand A in terms of the stress-strain, volumetric-axial strain and stiffness-strain responses. In Figure 19 only the stress-strain and volumetric-axial strain responses are presented, as the Sand B samples tested at high densities were not equipped with local instrumentation. Inspection of the figures shows that the state parameter-dependent model reproduces well the measured peak and post-peak stress-strain response of the two sands. In terms of the volumetric response, Calibration 2 reproduces well the measured response for the whole strain range, whilst Calibration 1 reproduces well the measured volumetric response for axial strains up to around 5% but significantly overpredicts the measured dilative strains thereafter. This is a result of the fact that Calibration 1 assumes a unique CSL defined on the basis of the looser samples (refer to Section **Error! Reference source not found.** and Figure 8). Figures 18 and 19 show that the larger predicted dilative strains in Calibration 1 result in post-peak stress-strain responses, which exhibit a slower reduction of deviatoric stresses than Calibration 2, i.e. higher deviatoric stresses at given values of axial strain, reaching the critical state angles of shearing resistance at significantly larger axial strains; well beyond the 20% achieved in the tests. Inspection of the stiffness-strain response presented in Figure 18 shows that the IC.3GS non-linear model reproduces well the response measured by the local instrumentation.

The simulations presented in Appendix A show that the state parameter-dependent model in combination with the IC.3GS non-linear model, both with a single set of input parameters, can reproduce well the measured stress-strain and volumetric response in tests with varying densities and stress states, with similar comments as above applying to the two calibrations. An exception is the stress-strain response of the test on Sand A carried out at D_r = 61% and p'_o = 50kPa (refer to Figure A.1). However, it is noted that the measured response for this test is not consistent with the other tests, as the measured peak stress is lower than the critical state strength obtained from the other tests. It is therefore reasonable to disregard this test from the calibration exercise.

Figures 20 and 21 present the predictions of the strain-softening Mohr-Coulomb model for the same CID tests shown in Figures 18 and 19 respectively. In addition, Appendix B presents the simulations of this model for the same CID tests presented in Appendix A. Figures 20 and 21 show that the strain-softening Mohr-Coulomb model predicts reasonably well the measured response of the two sands for the densities and confining pressures of these tests. Inspection of the simulations in Appendix B shows that, whilst the measured response is generally well reproduced for the tests with very high densities, i.e. D_r > 80%, the measured peak and volumetric response is not captured in some tests with lower densities (for example the tests with D_r = 76% and p'_o = 50kPa in Figure B.1 and D_r = 79% and p'_o = 200kPa in Figure B.2). It is noted that one set of parameters has been assumed for D_r = 60 - 80% and another set for D_r > 80%; denoted in Figure 14 and 15 as dense and very dense, respectively. It may be that the predictions of this model could have been improved with the introduction of further sets of parameters, particularly for the D_r = 60 - 80% density range. However, as the sand response depends not only on density but also on stress state, it is difficult to capture both effects with a limited number of sets of input parameters.

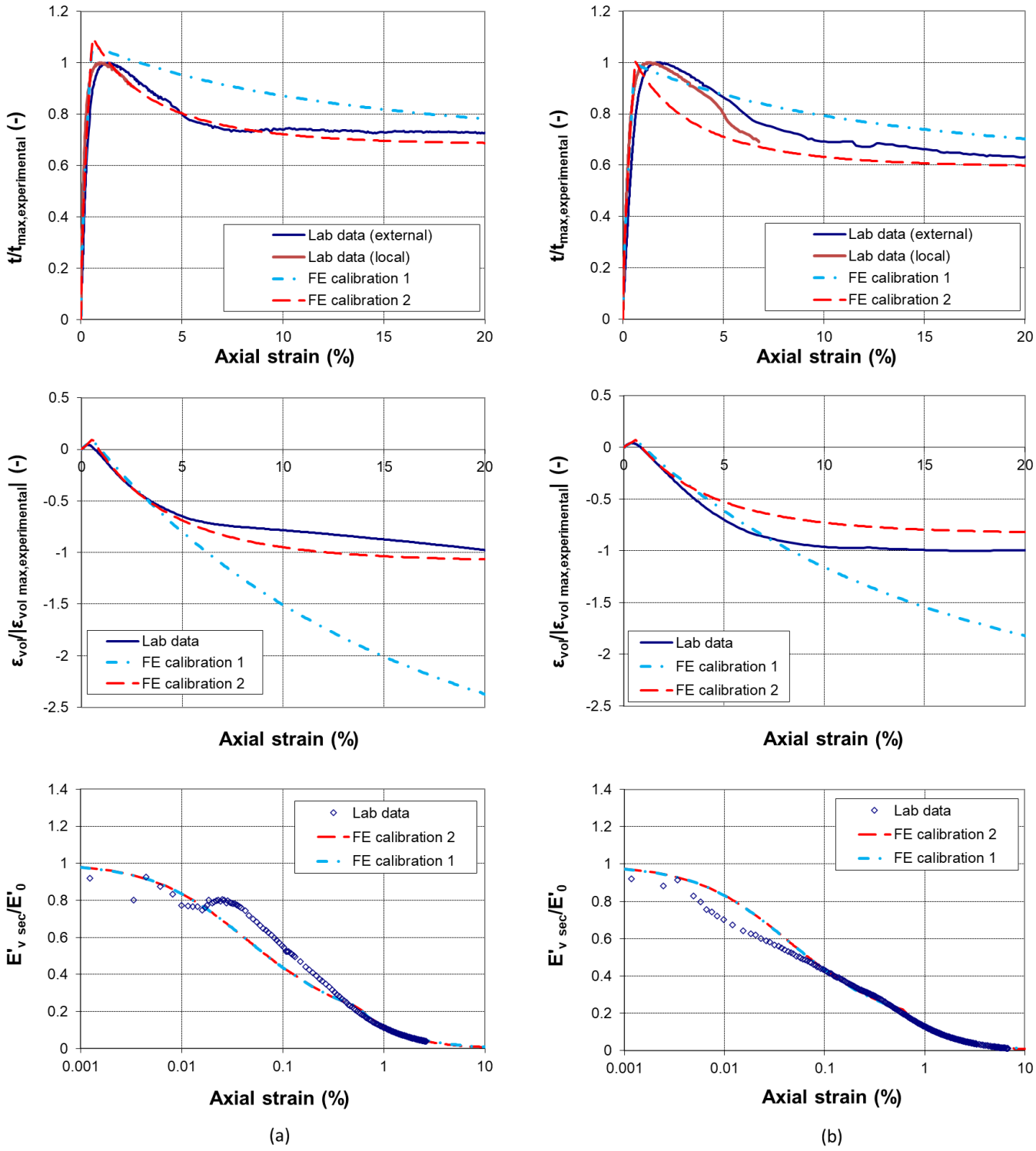

Figure 18. Comparison of experimental and simulated response using the state parameter-dependent model for Sand A a) D_r = 83% and p'_0 = 70kPa b) D_r = 88% and p'_0 = 80kPa

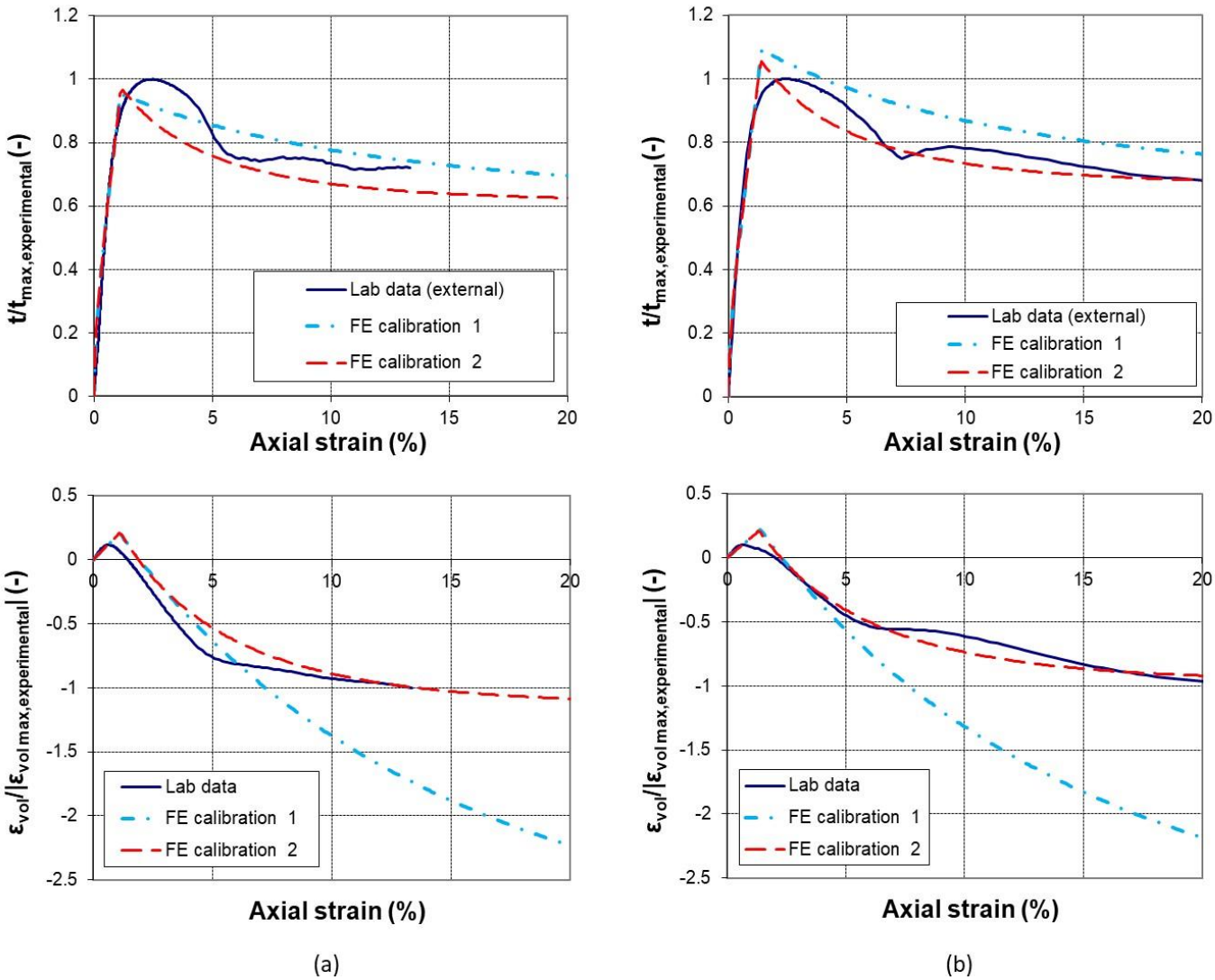

Figure 19. Comparison of experimental and simulated response using the state parameter-dependent model for Sand B a) D_r = 84% and p'_0 = 200kPa b) D_r = 94% and p'_0 = 300kPa

It is noted that in the stress-strain curves predicted by the strain-softening Mohr-Coulomb model in Figures 20 and 21 and Appendix B, three distinct zones of post-yield response can be observed, i.e. after the stress-state reaches the Mohr-Coulomb yield surface and the behaviour changes from non-linear elastic to elasto-plastic. These correspond to the three zones shown in Figure 14 and 15 for the variation of the angle of shearing resistance and dilation with the plastic deviatoric strain, E_d. When comparing the zones in Figures 14 and 15 with the stress-strain curves in Figures 20 and 21 and Appendix B, it is important to note that in triaxial conditions the axial strain corresponds to $E_d/\sqrt{3}$, e.g. E_d^p = 18% equates to a plastic axial strain of around 10%.

Comparison of the single element simulations using the strain-softening Mohr-Coulomb model with those using the state parameter-dependent model shows that the volumetric response predicted by the former are more akin to the predictions of the state parameter-dependent model using Calibration 2, rather than Calibration 1. This is not surprising, as Calibration 2 aimed to reproduce the volumetric response measured in the CID tests. It is noted though that whilst for the Mohr-Coulomb model the predicted stress-strain and volumetric response have been assumed to reach critical state at about 10% axial strains, for Calibration 2 the critical state is reached at larger axial strains, albeit still significantly smaller than for Calibration 1.

Appendix C presents a comparison between the measured and simulated stiffness-strain response for the advanced triaxial tests that were equipped with local instrumentation. The simulations are shown for the state parameter-dependent model. It can be seen that both calibrations result in the same predictions; these are also practically the same as the predictions with the strain-softening Mohr-Coulomb model (not presented herein for brevity), as for both models the pre-yield response is controlled by the non-linear elastic model IC.G3S. Figure C.1 shows that the IC.G3S model reproduces well the dependence of stiffness on density, stress-state and strain and the predictions provide an excellent match of the measured response for both Sand A and Sand B.

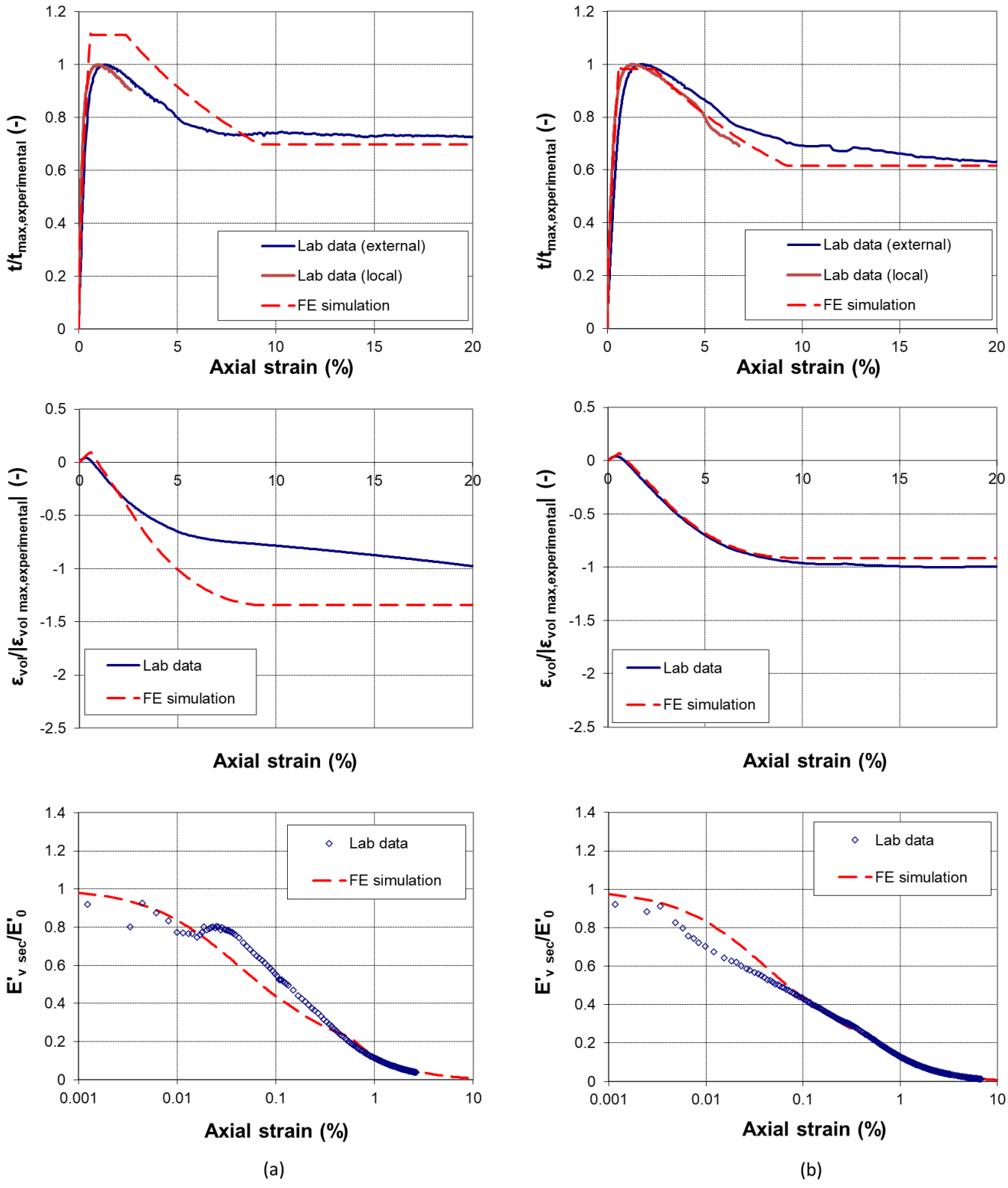

Figure 20. Comparison of experimental and simulated response using the strain-softening Mohr-Coulomb model for Sand A a) D_r = 83% and p'_0 = 70kPa b) D_r = 88% and p'_0 = 80kPa

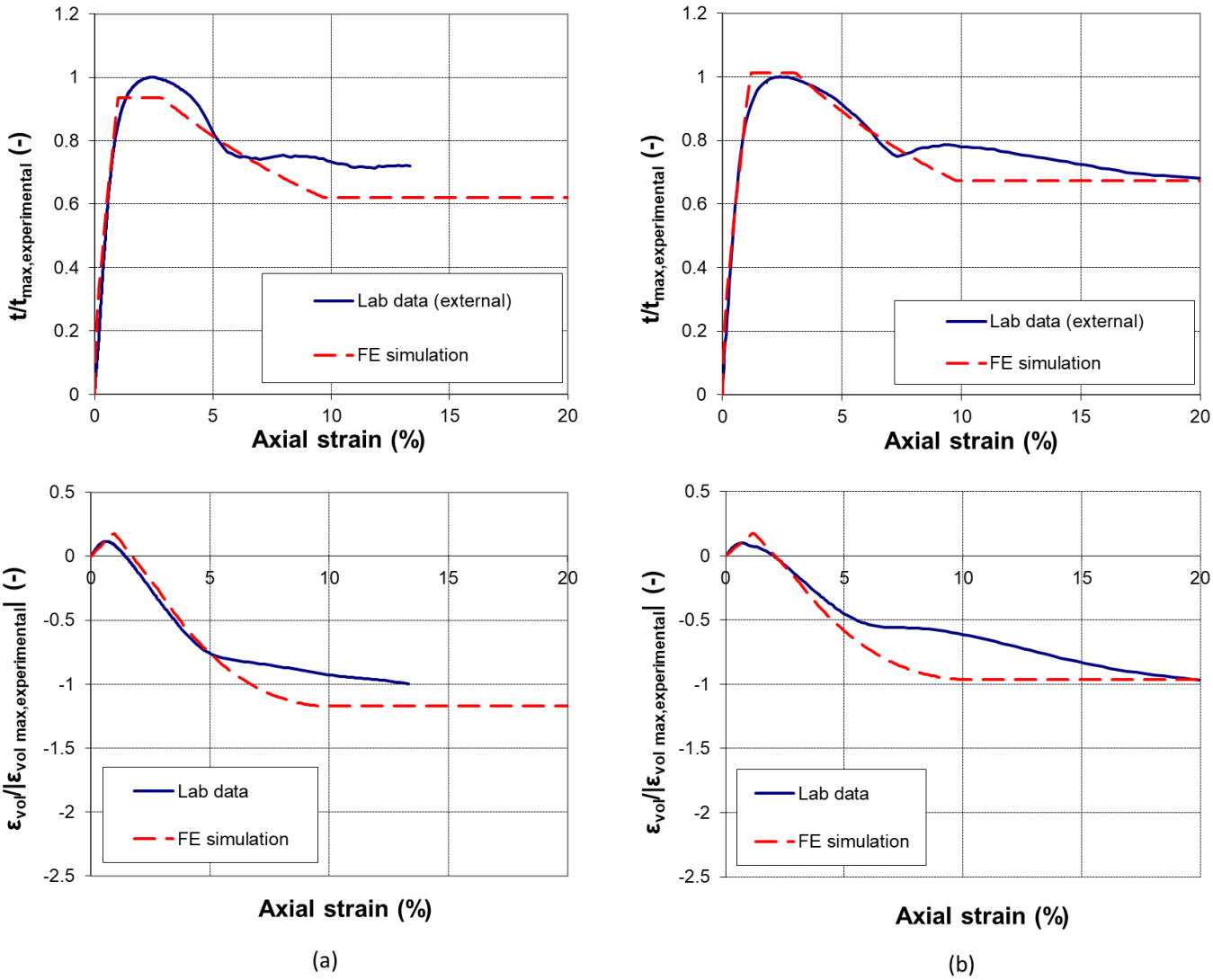

Figure 21. Comparison of experimental and simulated response using the strain-softening Mohr-Coulomb model for Sand B a) D_r = 84% and p'_0 = 200kPa b) D_r = 94% and p'_0 = 300kPa.

2.3 *Application in analysis of a monopile foundation*

2.3.1 *General*

The performance of the state parameter-dependent model, for the two calibrations of this model, and the strain-softening Mohr-Coulomb model were examined in the 3D FE analysis of an example monopile foundation from the sand-dominated offshore wind farm.

2.3.2 *Location specific parameter derivation*

As demonstrated in the previous section, the calibration of the constitutive models was carried out on the basis of the in-situ and laboratory tests from across the wind farm site. However, the application of the constitutive models in the 3D FE analysis of a particular monopile foundation is based on the CPTu profile at that WTG location.

Figure 16(a) presented the in-situ D_r profile at the example WTG location considered in the FE analyses presented herein; this profile was calculated on the basis of the interpretation of the CPTu test at that location. Figure 16(a) also showed the assumed idealised D_r profile. On the basis of this, the initial void ratio, e_0, used in the FE analysis of the monopile can be calculated (using, as previously discussed, the e_{min} and e_{max} values for each sand deposit). The initial void ratio, e_0, is important as it controls the state parameter, ψ, in the state-parameter dependent model, as well as the stiffness predicted by the non-linear model, IC.G3S, which is combined with both elasto-plastic models.

In the FE analysis using Calibration 1 of the state parameter-dependent model, a single set of model parameters was applied for each of the two sand deposits. However, in the FE analysis with Calibration 2, the input $e_{cs,ref}$ values were varied, on the basis of the idealised D_r profile shown in Figure 16(a), in order to obtain appropriate "shifted" CSL positions.

In the case of the strain-softening Mohr-Coulomb model, the idealised D_r profile was used in order to choose the appropriate input parameters to be applied in this model for the different sand units. As aforementioned, at this location Sand A is encountered in predominantly dense to very dense states, i.e. with the exception of the first 1.5m, $D_r \approx$ 60-95%, whilst Sand B is encountered at predominantly very dense states, i.e. $Dr \geq 80\%$. The variations of φ' and ν applied for both sands were those shown in Figures 14 and 15, with only the top layer of Sand A, in which $D_r < 60\%$, being modelled with a constant angle of shearing resistance, $\varphi' = \varphi'_{cs}$, and a zero angle of dilation, as discussed in Section 2.2.3.

It is noted that at a depth of about 10m there is a thin layer of silty Sand B. This has been modelled simplistically as a loose Sand B layer (i.e. with a constant angle of shearing resistance, $\varphi' = \varphi'_{cs}$, and a zero angle of dilation). In addition, there are some thin layers of clay which have been ignored in the analyses.

2.3.3 Details of analyses

The analyses were carried out using the FE code ICFEP. The finite element mesh adopted in the analyses is shown in Figure 22. It discretised only half of the problem as there is symmetry about the plane in which the horizontal load is applied. The analyses were based on small displacement finite element theory and employed quadratic elements, i.e. 20 node isoparametric hexahedral elements for the soil, 8 node isoparametric quadrilateral elements for the structural elements (Schroeder et al., 2007) and 16 node zero-thickness interface elements (Day and Potts, 1994) between the pile and the surrounding soil. Reduced 2x2 integration was used for all elements and a modified Newton-Raphson scheme with an error controlled sub-stepping algorithm was employed as the non-linear solver (Potts and Zdravkovic, 1999).

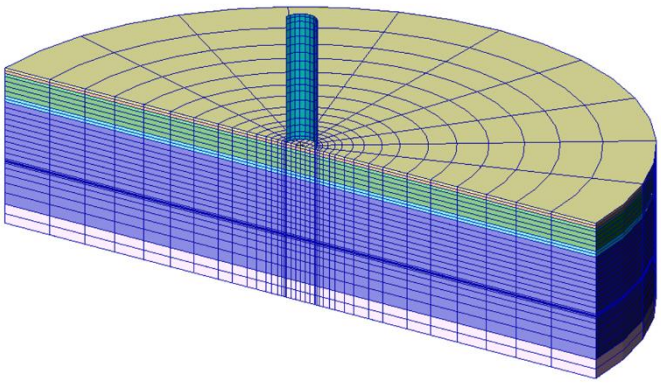

Figure 22. Finite element mesh adopted in analysis of example monopile foundation

The monopile and pile stick-up, which were incorporated in the FE model as hollow tubes, were assumed to behave as linear-elastic materials, with a Young's modulus of 205GPa and Poisson's ratio of 0.26. The interface elements were assumed to behave in a drained frictional manner with a strength described by an interface angle of shearing resistance between soil and steel equal to 25°.

The monopile was assumed to be wished-in-place at the start of the analysis, i.e. installation processes were not modelled in the analyses. The pore water pressures were assumed to have a hydrostatic distribution and the coefficient of earth pressures at rest K_0 was assumed to be equal to 1.0 at the beginning of the analyses.

Figure 23(a) presents profiles of the state parameter for the two calibrations of the state parameter-dependent model determined from the model parameters and the assumed initial conditions, i.e. stresses and sand density. On the basis of the state parameter profiles and the initial stresses, it is possible to estimate profiles of the peak angle of sharing resistance and dilation, corresponding to the drained triaxial compression (TXC) mode of shearing (assuming negligible elastic strains), see Figures 23(b) and 23(c). It can be seen that at high relative densities (see Figure 16(a)) and relatively small stresses, e.g. at a depth of about 4m for Sand A and a depth of about 10m for Sand B the state parameter has the most negative values for both calibrations (see Figure 23(a)). These result in high values of the peak angle of shearing and dilation, e.g. for Calibration 2 at a depth of about 4m the peak angle of shearing resistance and dilation for triaxial compression conditions are estimated to be approximately 50º and 28º respectively. It is noted that CID tests were not available at corresponding confining pressures and densities to check these calculated peak values. However, these values were considered to be very high, and in the monopile FE analyses limiting cut-off values were applied, i.e. $\varphi'_{max} = 45°$ and $\nu_{max} = 25°$ for Sand A and $\varphi'_{max} = 45°$ and $\nu_{max} = 20°$ for Sand B. These values are indicated in Figure 23(b) and Figure 23(c).

It is important to note that the calibration of the constitutive models was undertaken on the basis of triaxial compression tests, for which the Lode's angle, θ, is constant and equal to -30º. However, in the 3D FE analysis the value of θ will vary and it is not possible to determine this a priori. In the constitutive models used in this work, a Mohr-Coulomb hexagon, and hence a constant of angle of shearing resistance, has been assumed in the deviatoric plane. However, ideally, laboratory tests should be carried out at different values of the Lode's angle, from which the variation of the angle of shearing resistance with θ can be established.

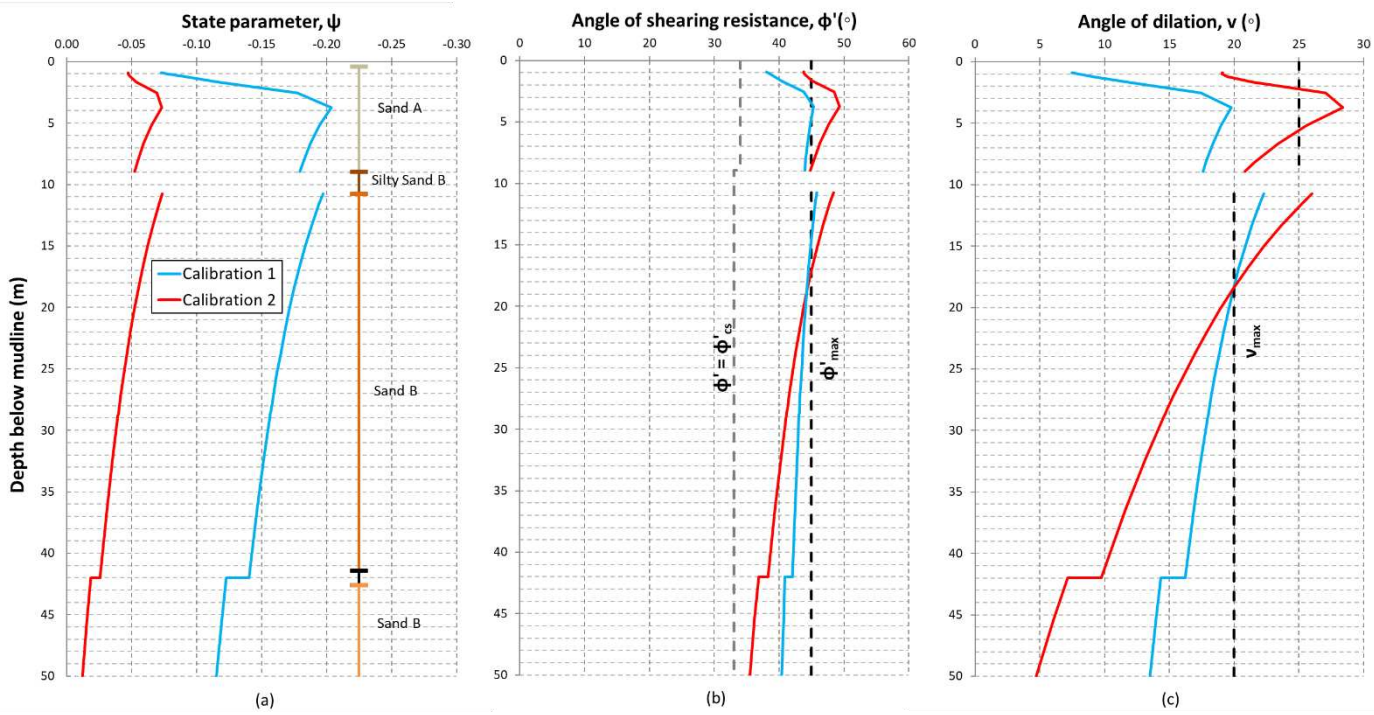

Figure 23. Profiles of a) the state parameter b) peak angle of shearing resistance in TXC c) peak angle of dilation in TXC

It is recognised that the use of strain-softening constitutive models in the analysis of boundary value problems, like the response of monopiles to lateral and moment loading considered herein, leads to a significantly increased mesh dependency. Although non-local methods, which reduce mesh dependency, exist in ICFEP (Summersgill et al., 2017a, 2017b), these methods were not adopted in this work, and a sensitivity study with different mesh sizes was carried out to confirm the appropriateness of the chosen mesh discretisation.

2.3.4 Results of analyses

Figure 24 presents the results of the FE analyses using the state parameter-dependent model (for both Calibrations 1 and 2) and the strain-softening Mohr-Coulomb model, in terms of horizontal load-displacement curves of the monopile at seabed level. The horizontal load in this figure is normalized by the load predicted by the strain-softening Mohr-Coulomb model at a horizontal displacement equal to 10% of the monopile diameter (a displacement that is commonly assumed to represent failure).

Figure 24(a) shows the predicted initial response of the monopile up to seabed displacements equal to 2%D (where D is the monopile diameter), whereas Figure 24(b) presents the predicted overall response of the monopile up to horizontal displacements equal to 20%D. In the former figure, it can be seen that the two calibrations of the state parameter-dependent model predict practically the same initial monopile response which is also very similar to that predicted by the strain-softening Mohr-Coulomb model. This is not surprising as all three analyses use the same non-linear elastic model.

However, at higher seabed displacements, Calibration 1, which assumes a unique position of the CSL on the basis of the relatively loose samples, results in considerably higher predicted loads than Calibration 2, in which the position of the CSL is assumed to depend on relative density. This is line with the fact that Calibration 1 results in significantly higher dilative strains than Calibration 2, as discussed in the previous sections. Figure 24(b) shows that the load predicted at a horizontal displacement equal to 10%D with Calibration 1 is 13% higher than the one predicted with Calibration 2; this difference increases with increasing displacements to 18% at displacements of 20%D. It is clear that the assumptions made in relation to the critical state line have a significant impact on the predicted monopile response, even if varying the CSL position is somewhat compensated by using different values of k and l. Moreover, although not presented herein, there are also differences in the soil-reaction curves extracted from these analyses. This would in turn impact monopile designs across the OWF, as it would affect the relationships adopted in the 1D beam-spring models in the application of the PISA design methodology. It is noted that these findings are not limited to the state parameter-dependent constitutive model chosen in this work but would apply to any state parameter-based model based on the critical state framework.

Comparison of the results from the state parameter-dependent model with those from the strain-softening Mohr-Coulomb model in Figure 24(b) shows that the predictions of the latter are closer to the predictions of the state parameter-dependent model for Calibration 2. Again, this is in line with the single element simulations presented previously and the fact that Calibration 2

aimed to reproduce the volumetric response measured in the CID tests, on which the Mohr-Coulomb model calibration was based. The difference between these two analyses are in the order of 5% and 10% at displacements of 10%D and 20%D, respectively. However, it is important to note that for this monopile location, at the depths relevant to the monopile analyses (i.e. depths less than 40m) the density at which the two sand deposits are encountered is practically constant, with the only exception of the top 2m (in which the soil resistance is low, due to the small effective stresses). As such, it is likely that in a location with varying sand density, larger differences would exist between the strain-softening Mohr-Coulomb and the state parameter-dependent model for Calibration 2, as the former is not as versatile as the latter in capturing the effects of both varying density and stress state.

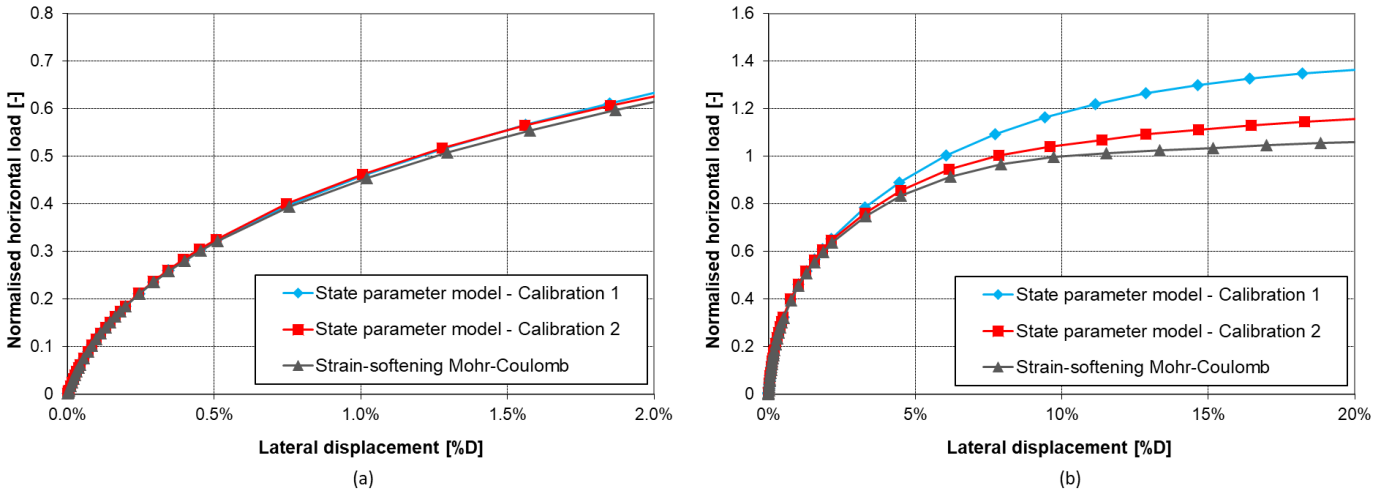

Figure 24. Load displacement curves at design seabed level a) initial response b) overall response

2.4 *Study on parameters of Mohr-Coulomb model*

In addition to the analyses presented above, a study was carried out regarding the choice of parameters for the Mohr-Coulomb model. In this study the angle of shearing resistance was assumed to be constant and the angle of dilation was assumed to either i) vary as shown in Figure 14, ii) be constant and equal to the peak value shown in Figure 14, or iii) be constant and equal to zero. The analyses were repeated for two constant angles of shearing resistance, as follows a) φ'_{peak}, and b) φ'_{cs}. The results of these analyses are presented in Figure 25(a) and Figure 25(b) for $\varphi' = \varphi'_{peak}$, and $\varphi' = \varphi'_{cs}$, respectively. These figures show that there are large differences in the predictions depending on the assumed dilation. Differences of up to 20% at displacements of 10%D and 40% at 20%D are shown in Figure 25(a) for constant values of dilation equal to zero and peak values. Smaller differences can be seen in Figure 25(b). As expected, the predictions of the analysis with varying dilation plot in between the two analyses with constant dilation in Figures 25(a) and 25(b). However, the analysis with varying dilation either overpredicts in Figure 25(a) or underpredicts in Figure 25(b) significantly the monopile response as compared to the predictions of the strain-softening model from Figure 24, which proves that it is not possible to make an a priori decision as to which approach is conservative and demonstrates the necessity of simulating the variations in both the angle of shearing resistance and dilation.

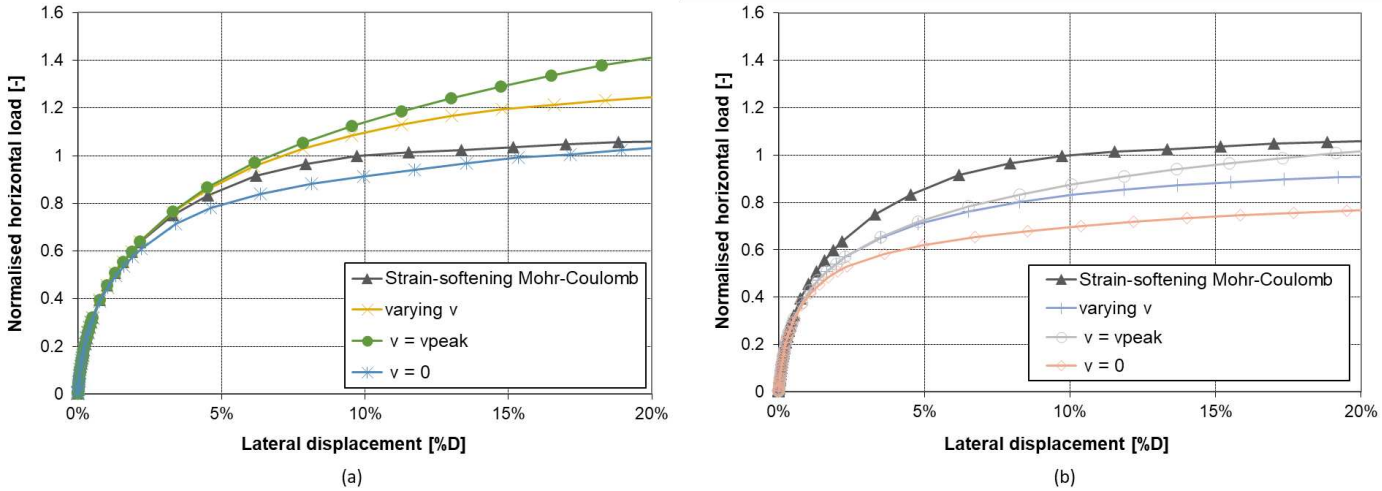

Figure 25. Load displacement curves at design seabed level for Mohr-Coulomb model a) $\varphi' = \varphi'_{peak}$ b) $\varphi' = \varphi'_{cs}$

3 MODELLING STIFF CLAYS

Stiff clay deposits are commonly encountered at both onshore and offshore sites. At Northern European offshore sites stiff clays are often found in the form of ablation tills deposited during glacial periods, as well as clay formations deposited in a variety of other depositional environments, e.g., glaciomarine/marine, lacustrine, estuarine/intertidal, etc. This can result in materials with significantly different characteristics and, as OWF sites generally cover large areas, it is not unusual to encounter a variety of clay formations at any one site. In addition, there can be significant variability within each formation/deposit itself.

When modelling stiff clay deposits, it is important to establish the key facets of their behaviour and assess the potential variability of a given clay layer across the site. In many instances the clay's plasticity is a key index property as it has a significant impact on the shearing response of stiff clays.

The work presented herein examines some of the key differences of stiff clays with low and high plasticity and discusses ways in which important facets of their response can be modelled using appropriate constitutive models. Furthermore, it demonstrates the derivation of model parameters on the basis of high-quality in-situ and laboratory investigations from offshore wind farm sites.

3.1 Stiff clays with low plasticity

Glacial tills are most commonly found to be low plasticity stiff clay deposits which exhibit significant dilation and a ductile stress-strain response reaching critical state conditions, when sheared undrained in compression. Constitutive models based on the critical state framework, such as the Modified Cam Clay model (MCC) proposed by Roscoe and Burland (1968) are therefore an obvious choice to capture the behaviour of such materials.

Glacial tills are commonly encountered at OWF sites across Northern Europe and one example of such a material is the Cowden till, which was studied in the PISA research project. In the PISA work, the behaviour of the Cowden till was simulated with an enhanced version of the MCC model, as described by Zdravkovic et al. (2020b). This model featured i) a non-linear Hvorslev surface on the dry side (Tsiampousi et al., 2013), ii) a generalised shape for the yield and plastic potential surfaces in the deviatoric plane (Van Eekelen, 1980) and iii) a strain dependent non-linear shear response pre-yield, described by the IC.G3S model (Taborda et al., 2016). Figure 26 shows the yield surface of the model in p'-J plane (where J is the generalised deviatoric stress) and Table 6 summarises the model parameters. The equations and further details of the model are provided by Zdravkovic et al. (2020b).

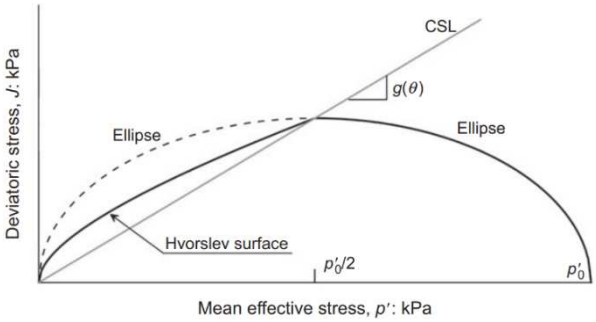

Figure 26. Yield surface in the p´ –J plane of the enhanced modified Cam Clay model adopted in the PISA work (from Zdravkovic et al. 2020b)

The same enhanced version of the MCC model has been used by the authors to reproduce successfully the response of low plasticity clays at element level and has been adopted in 3D FE analyses carried out as part of the design process for a number of OWFs across Northern Europe (Grammatikopoulou et al., 2017, 2020; Schroeder et al., 2020).

The Bolders Bank Formation (BDK) is an example of such a low plasticity clay. It is an ablation till, deposited during the Weichselian glacial period, and its response is similar to Cowden Till. For the OWF site discussed by Schroeder et al. (2020), the experimental data indicated that the BDK should be split into upper and lower sections, BDK(U) and BDK(L), with the latter being generally stiffer and stronger. The parameter derivation and calibration of the enhanced MCC model for these materials, on the basis of advanced laboratory testing on samples from across the wind farm area, is outlined in the following paragraphs.

In the first instance the MCC parameters λ, κ and v_I were derived from available oedometer tests. As an example, Figure 27 presents typical oedometer test data re-plotted in v-ln(p') space for a) a Constant-Rate-of-Strain (CRS) test and b) an Incremental Loading test. In the MCC model the isotropic compression and swelling lines are assumed to be straight, described by the slopes λ and κ respectively. Figure 27 shows that, at high stresses (corresponding to normally consolidated states) it is appropriate to approximate the isotropic compression line as a straight line defined by a constant value of λ. However, unlike the isotropic compression line, the swelling line is generally curved, as shown in Figure 27(a). Therefore, some judgement is required when choosing a constant value of κ to reasonably represent the swelling line obtained from oedometer tests. It is worth noting that the curved nature of the swelling line is not always captured well in incremental loading tests, particularly if relatively large initial unloading steps are used (see Figure 27(b)).

Table 6. Summary of parameters of enhanced Modified Cam Clay model adopted in PISA study (see Zdravkovic et al., 2020b)

Parameter	Description
v_1	Specific volume of isotropic compression line at p' = kPa
λ	Slope of isotropic compression line in v -lnp' *space*
κ	Slope of swelling line in v -lnp' *space*
X, Y and Z	Parameters defining the critical state strength and the shape of the yield surface in the deviatoric plane
a and m	Paremeters defining the shape of the non-linear Hvorslev yield surface
β and m	Paremeters defining the plastic potential associacted with the non-linear Hvorslev yield surface
G_0, p'_{ref}	Parameters defining the elastic shear modulus at small strains
a, b and $R_{G,min}$	Parameters defining the degradation of the elastic shear modulus

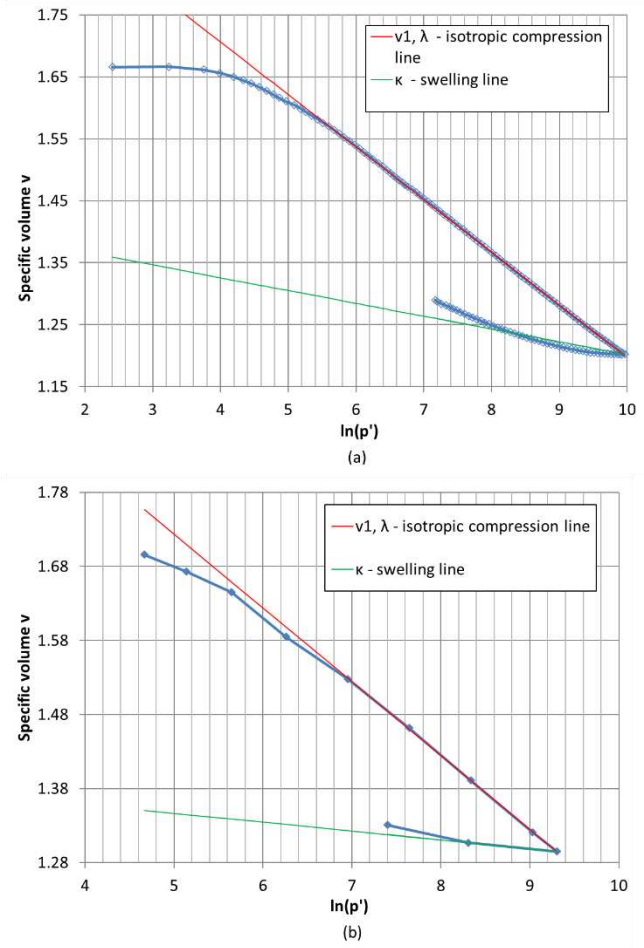

Figure 27. Derivation of parameters λ, κ and v_1 from oedometer tests a) CRS test b) Incremental loading test

The required critical state angle of shearing resistance and its variation with Lode's angle θ can be established on the basis of undrained triaxial compression CAUc and extensions CAUe tests. Figure 28(a) shows the peak and ultimate stress states obtained at the end of the tests on samples of BDK(U) and BDK(L), together with envelopes corresponding to the chosen angles of shearing resistance in triaxial compression (TXC) and extension (TXE). In compression the tests have a ductile response with ultimate and peak stress-states being identical (hence the absence of peak stress-states in the figure). The ultimate states of the tests show a well defined critical state line facilitating the choice of an appropriate critical state angle ($\varphi'_{cs,TXC}$). However, for the limited number of available extension tests, the ultimate stress states are lower than the peak stress states in most tests. This is thought to be due to the non-uniform stress conditions induced by "necking" failures which often occur in this type of test. It is therefore considered appropriate to ignore the ulimate stress states and choose an appropriate critical state angle in extension ($\varphi'_{cs,TXE}$) on the basis of the peak stress states of the relevant extension tests.

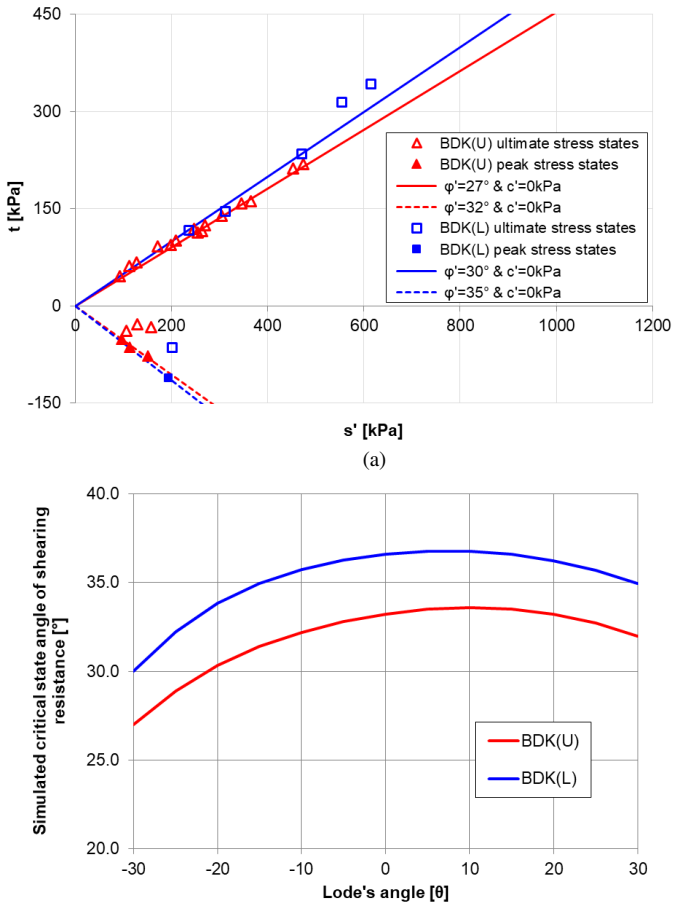

Figure 28. Derivation of critical state parameters for BDK(U) and BDK(L) a) CAU tests and assumed φ'_{cs} in triaxial compression and extension b) Assumed variation of φ'_{cs} with the Lode's angle, θ (from Schroeder et al., 2020)

The envelopes shown in Figure 28(a) correspond to $\varphi'_{cs,TXC} = 27°$ and $\varphi'_{cs,TXE} = 32°$ for BDK(U) and $\varphi'_{cs,TXC} = 30°$ and $\varphi'_{cs,TXE} = 35°$ for BDK(L). Hence, in both units the strength in triaxial compression is lower than the strength in triaxial extension; an important aspect of their behaviour that should be modelled. As no information was available regarding the strength of the material for values of Lode's angle, θ, other than $\theta = -30°$ (TXC) and $\theta = 30°$ (TXE), the shape of the yield surface in the deviatoric plane for BDK(U) was assumed to be the same as that adopted for Cowden Till in the PISA project (Zdravkovic et al., 2020b), noting that both materials have the same strength in triaxial compression and extension. This results in the variation of the critical state angle of shearing resistance with θ shown in Figure 28(b). As shown in this figure, for BDK(L) a similar shape was adopted, which ensured that the strength in triaxial compression and extension matched the values of $\varphi'_{cs,TXC} = 30°$ and $\varphi'_{cs,TXE} = 35°$ determined from the relevant triaxial tests. The plastic potential for both units was assumed to have the same shape as the yield surface in the deviatoric plane.

Examination of the triaxial compression and extension stress paths suggested that the use of a non-linear Hvorslev type yield surface on the dry side would be appropriate. Comparison of single element simulations with test data on both BDK(U) and BDK(L) samples confirmed that the shape of the Hvorslev surface for these materials is similar to that adopted for the Cowden Till in the PISA work. The plastic potential associated with the Hvorslev surface was assumed to be linear, as for the Cowden Till (i.e. $m = 1.0$ was adopted, after Zdravkovic et al. (2020b)). The amount of dilation relating to the Hvorlsev surface, which is governed by the parameter β, was also derived on the basis of single element simulations of the undrained triaxial tests.

The variation of the pre-yield shear stiffness with strain was derived on the basis of advanced triaxial tests with local instrumentation which allowed the measurement of stifness from very small strains. Figure 29 presents the variation of the normalised secant undrained Young's modulus, E_u, with shear strain invariant, ε_s ($\varepsilon_s = E_d/\sqrt{3}$), obtained from undrained triaxial compression tests on BDK(U) (it is noted that ε_s is equal to axial strain in undrained triaxial tests). The triaxial tests also included the measurement of the G_{vh}, G_{hv} and G_{hh} stiffness at very small strains, using multi-axis bender elements. However, the results of these tests were very variable (i.e. the normalised E_u values varied between about 500 and 7000) and hence are not presented in Figure 29. The bender element tests, as well as the stress paths measured in the triaxial tests indicated some limited stiffness anisotropy. However, as the available tests were not sufficient to fully define the stiffness anisotropy of the material, it was considered appropriate to assume isotropic stiffness in modelling the BDK materials (hence $E_u = 3G$ in Figure 29). Figure 29 also shows the idealised stiffness curve derived for BDK(U) on the basis of the available data. The idealised shear stiffness curve for BDK(L) was derived in a similar manner.

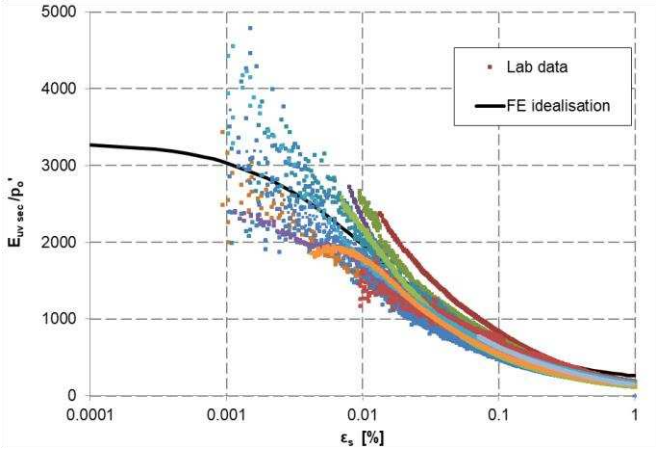

Figure 29. Stiffness-strain curve on the basis of CAU tests and idealised response for BDK(U) (from Schroeder et al., 2020)

It is noted that it is important to compare the stiffness reponse determined by laboratory tests (e.g. local instrumentation in triaxial tests, bender elements and resonant column tests) with that indicated by field measurements, such as seismic cone tests (SCPTs), cross-hole and down-hole geophysical testing, P-S logging tests etc.

The applicability of the adopted parameters to reproduce the response of the BDK(U) and BDK(L) materials at the OWF site was examined in single element FE simulations of individual triaxial tests. While all the parameters discussed above remained unchaged for all single element simulations, the initial K_0 values in the simulations were chosen to match the stress conditions of each sample at the beginning of undrained shearing, and the yield stress ratio, *YSR*, was chosen to replicate the undrained shear strength, S_u, measured in each test. As an example, Figure 30 compares the results of a typical CAUc test on BDK(U) with the predictions of the single element FE simulation of this test, in terms of stress-strain, effective stress path, pore water pressure-strain and stiffness-strain response. This shows that the enhanced MCC model, with the parameters derived in the manner set out above, reproduces well the ductile stress-strain response of the clay during shearing, as well as the dilative excess pore water pressure response. The effective stress path is also well-captured owing to the Hvorslev type surface adopted in the model on the dry side. Finally, the combination of the MCC model with the non-linear IC.G3S model result in an excellent reproduction of the stiffness-strain curve measured in the test.

Whilst the parameter derivation and calibration of the enhanced MCC model was carried out on the basis of site wide testing, the application of the model in 3D FE analysis of individual monopile foundations needs to be undertaken on the basis of CPTu profiles which are usually available for all WTG locations (similar to the work on sands presented in the previous section). In particular, the location specific 3D monopile analyses have to reproduce appropriate undrained strength profiles.

As an example, Figure 31(a) shows the undrained strength profiles for a particular WTG location, calculated from the location specific CPT test, using N_{kt} values of 15 and 20. These N_{kt} values were 'site-calibrated', on the basis of laboratory tests from across the OWF site, to give upper and lower bounds of undrained strength.

In addition to the Bolders Bank Formation, Figure 31 shows that two more formations were encountered at this location: the Egmond Ground Formation (EG), which is a dense marine sand and the Sand Hole Formation (SH), which, at this site, comprises stiff clays of low plasticity. The constitutive model choices, as well as the derivation and calibration of the model parameters for these materials followed similar principles to those set out in this paper. For brevity these are not discussed here.

In the MCC model, it is possible to calculate the undrained strength predicted by the model, on the basis of the input parameters of the model, the initial stresses (calculated in this case on the basis of the assumed submerged unit weight and K_0) and *YSR* (Potts and Zdravkovic, 1999). As such, a *YSR* profile with depth was chosen for this monopile location, shown in Figure 31(b), which, in combination with the MCC model parameters and the initial stress distribution, resulted in the undrained strength profile predicted by the model in triaxial compression, shown in Figure 31(a) and denoted as $S_{u,TXC\ (MCC)}$.

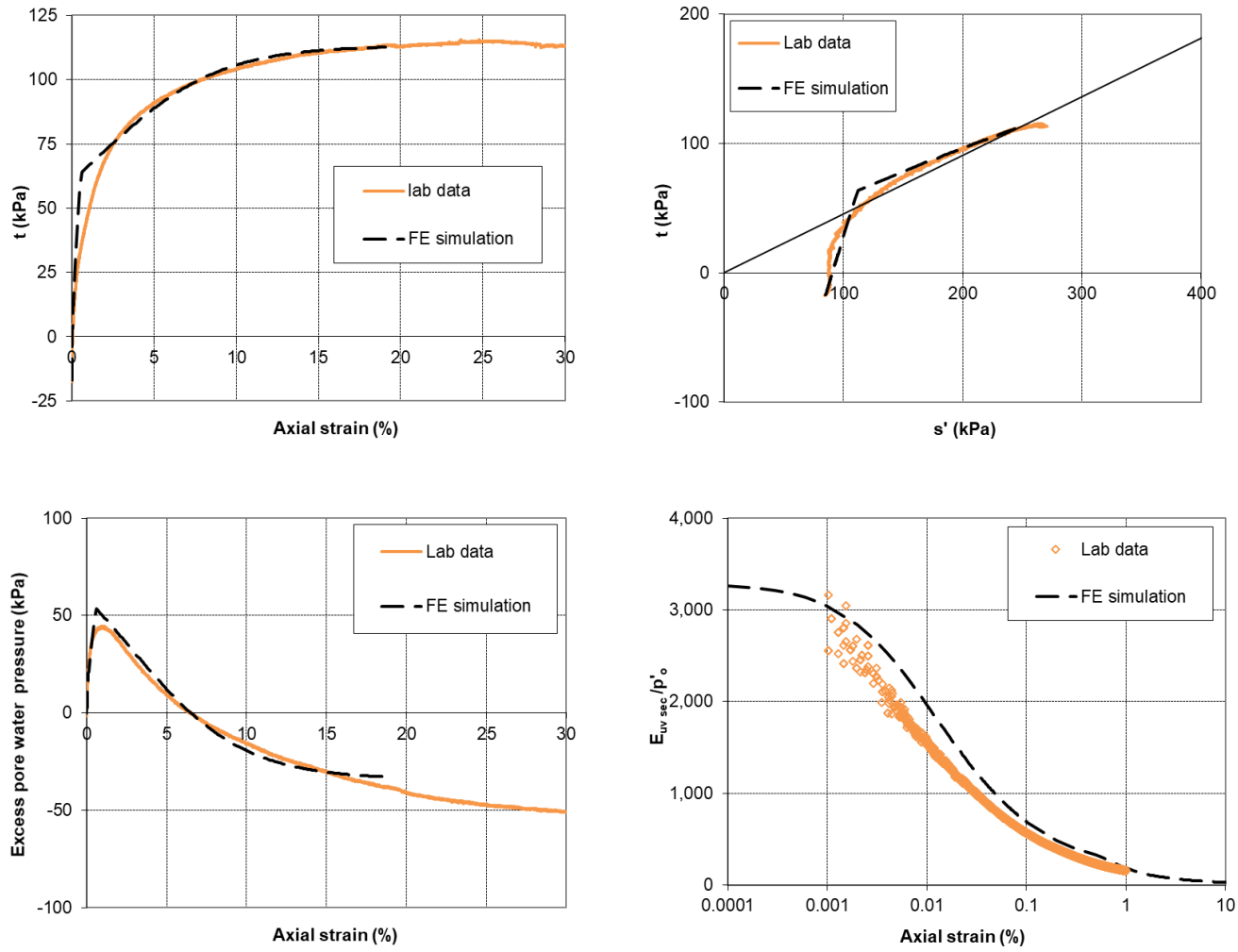

Figure 30. Comparison of experimental and simulated response for a CAUc test on BDK(U) (from Schroeder et al., 2020)

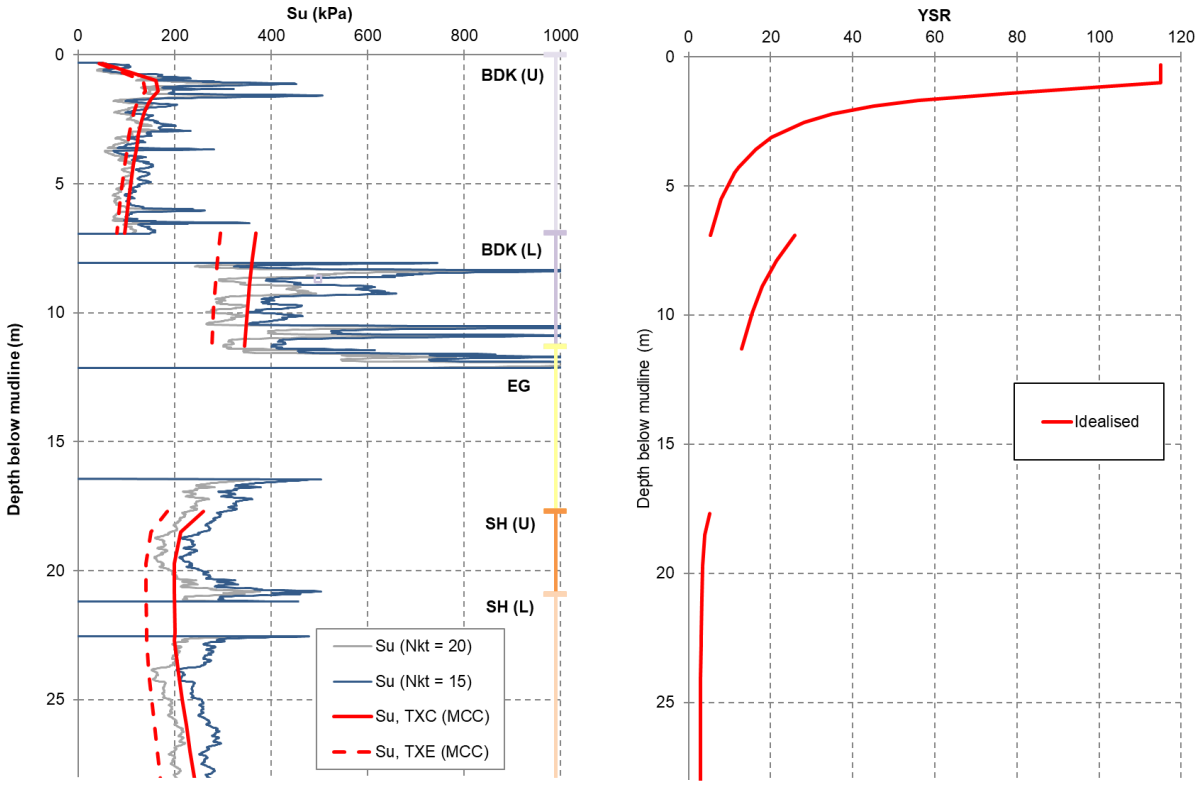

a) b)

Figure 31. a) Undrained strength profiles b) Assumed YSR profile

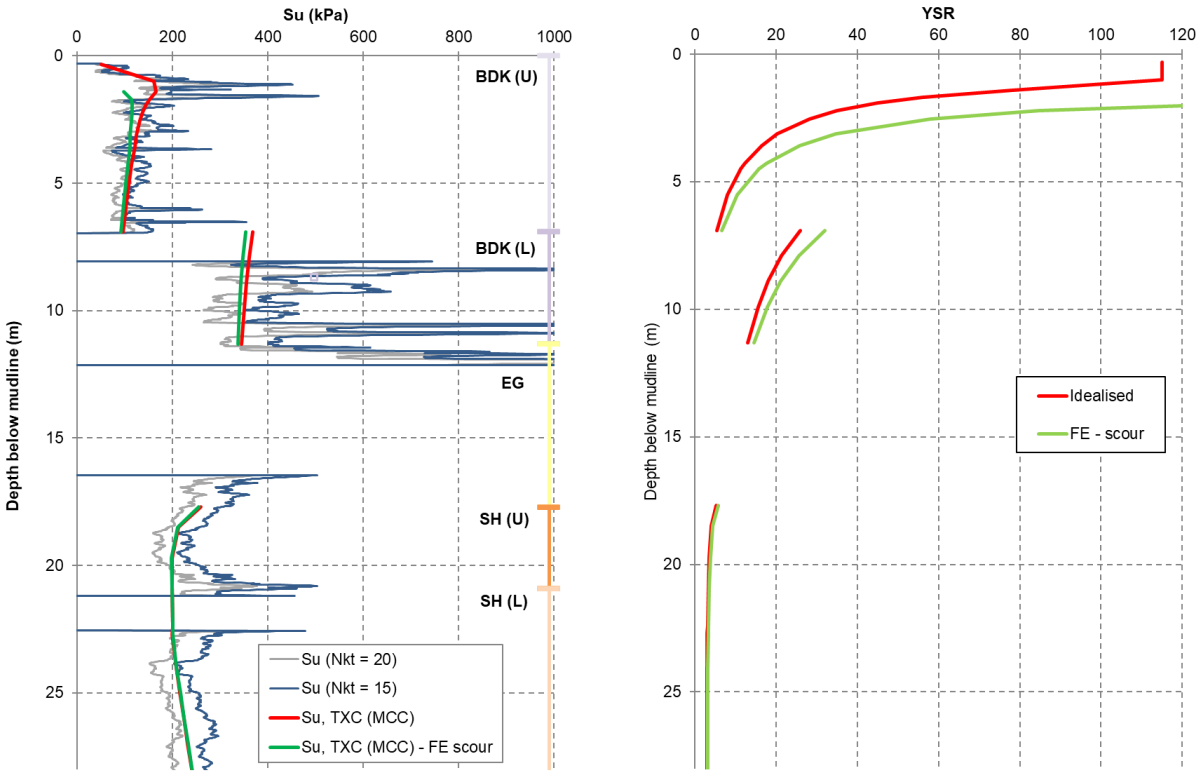

a) b)

Figure 32. a) Undrained strength profile b) Assumed YSR profile adopted in FE analysis with scour

It is noted that the undrained strength profile predicted by the model in triaxial extension (also shown in Figure 31(a)), or any other value of the Lode's angle, θ, will be different to the triaxial compression strength profile as it depends on the shape of the yield and plastic potential surfaces assumed in the deviatoric plane. This represents a challenge when applying the MCC model (and isotropic variants of the model) in 3D FE analysis. Whilst in plane strain analyses it is possible to determine the Lode's angle, θ at failure, predicted by the MCC model (on the basis of the yield and plastic potential deviatoric shapes, Potts and Gens (1984)) and hence the corresponding undrained strength mobilised in the FE analysis of the boundary value problem (Grammatikopoulou et al., 2007), this is not possible in 3D FE analyses. Hence, it is of paramount importance that the shapes selected for the yield and plastic potential surfaces in the deviatoric plane produce a realistic variation of the clay's strength with the Lode's angle, θ. In order to do so it is necessary to have appropriate laboratory tests from which these variations can be derived, which represents a challenge on its own.

Using the critical state framework, it is possible to include effects of any anticipated global scour at a particular WTG location in a consistent manner, recognising that the undrained strength calculated on the basis of the CPTu data (Figure 31(a)) refers to an unscoured seabed. For the specific WTG location considered herein 1.3m of global scour, i.e. an overall lowering the level of the original seabed, was to be incorporated in the design. Consistent with the MCC model, this leads to changes in the undrained shear strength profile compared to that obtained from the unscoured CPT, as a result of changes to the *YSR*. The *YSR* following the assessed scour can be calculated by changing the initial vertical stress, as a result of global scour, and maintaining unchanged vertical yield stresses (see Figure 32(b)). The revised *YSR* profile (denoted as 'FE-scour') can then be used to calculate a new undrained strength profile consistent with the assessed scour.

3.2 Stiff clays with high plasticity

As previously discussed, variations in the plasticity of stiff clays can affect significantly their response to shearing. It is therefore important to carefully characterise any stiff clay formation encountered focussing on their index properties and any recognisable spatial variations.

As an example, Figure 33 presents profiles of index properties with depth and the corresponding plasticity chart for a given clay formation, encountered at a North Sea OWF site (Grammatikopoulou et al., 2020). All the data presented in Figure 33 are for the same clay formation, which was identified as consisting of channel infill materials, deposited in lacustrine to shallow marine sub-glacial conditions.

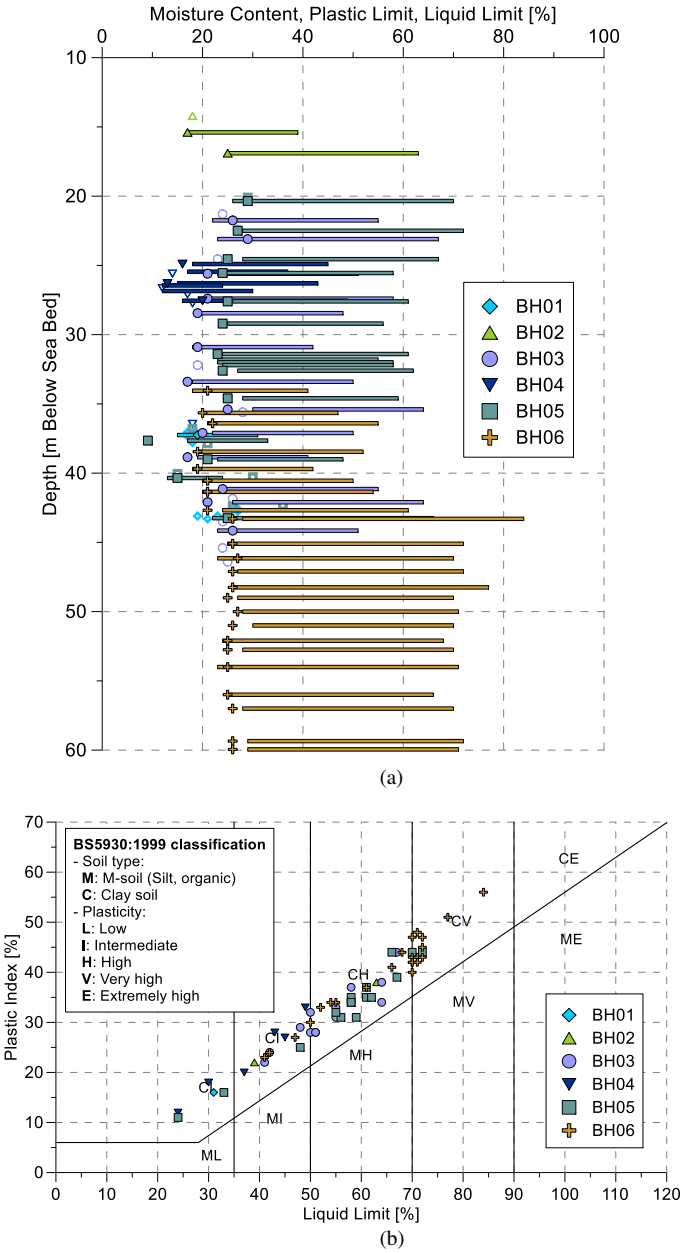

Figure 33. a) Profiles of index properties and b) Plasticity chart for Channel infill material

The graphs in Figure 33 indicate considerable variability of the plasticity of this clay formation, even within the same borehole. For example, in BH06 the plasticity index (PI) varies from about 20% to just over 55%. As expected, the response of this clay in undrained triaxial was found to be variable. In some cases, the material showed a ductile strain-stress response akin to a low plasticity stiff clay, i.e. similar to the one shown in Figure 30. In other cases, the material exhibited a brittle stress-strain response akin to a stiff overconsolidated plastic clay, i.e. when sheared it showed a peak strength which was followed by a drop to a "post-rupture" strength. Figure 34 shows an example of such a response for a sample from this site, whilst Figure 35 shows an example of the response of a sample from the same formation from a neighbouring site.

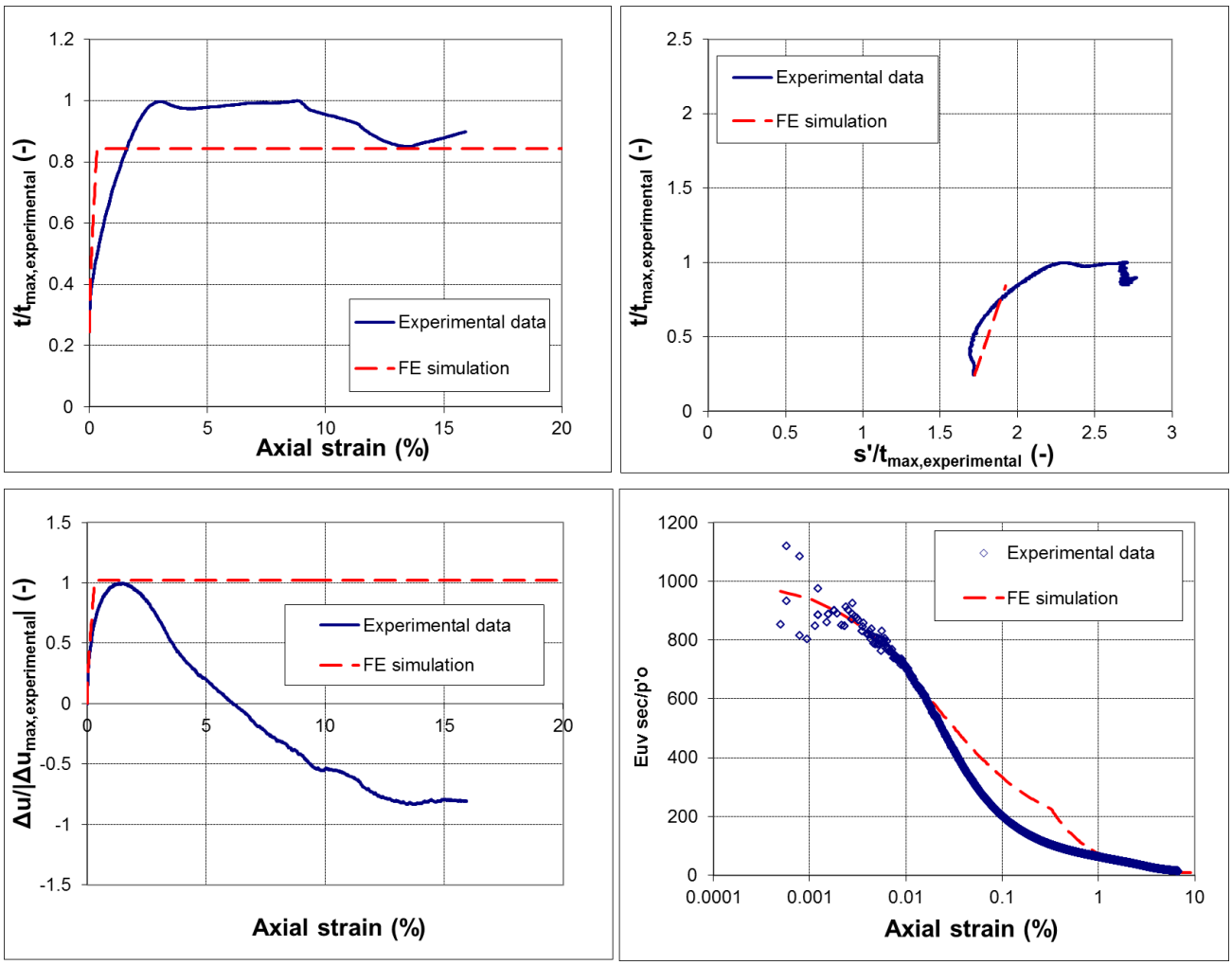

Figure 34. Comparison of experimental and simulated response for a CAUc test on stiff plastic clay – Channel infill material (from Grammatikopoulou et al., 2020)

In the first instance, the modeller therefore has to decide how to account for such variability and make appropriate choices as to whether to treat the material as low plasticity or high plasticity clays. Ideally, sufficient information would be gathered to split the formation into high and low plasticity material and then adopt different modelling strategies for each sub-unit. However, in the case of OWFs, it is uncommon to have boreholes, and consequently samples, for each WTG location; hence decisions have to be made on the basis of CPTu data only. Although CPT correlations and classification charts exist, it is not always clear from this type of test whether stiff clays are of low plasticity, and hence exhibit a response akin to that shown in Figure 30, or of high plasticity, and hence exhibit a response akin to that shown in Figures 34 and 35. As such, it is important that a sufficiently large number of laboratory tests are carried out to characterise each formation and that the measured response is examined carefully by the modeller before choosing the type of constitutive model to best represent the behaviour of the clay deposits encountered. If the variability of the material is found to be significant, then a conservative approach would need to be adopted.

Still, the modelling of stiff plastic overconsolidated clays poses significant challenges, as, contrary to low plasticity clays, they do not dilate to a unique critical state and hence exhibit non-critical state ultimate conditions. As such, it may not be appropriate to use the MCC model, in the form used for the low plasticity clays, as it would predict ductile hardening and, with a reasonable choice of *YSR*, would result in an overestimation of the strength of these clays. In addition, the MCC model cannot capture the brittle response of this type of clays.

One option would be to use a simple Mohr-Coulomb type model, in which $\varphi' = 0$ and c' equal to the undrained strength are assumed, i.e. like a Tresca model, but combined with a non-linear elastic model. Figures 34 and 35 show the results of a single element FE simulation using this type of model, in which c' equal to the post-peak undrained strength was adopted. As expected, the model cannot capture the brittle strain-softening response of the material, but with this choice of undrained strength, the simulations provide a conservative representation of the stress-strain response. However, the measured stress path and pore pressure response cannot be reproduced accurately. As for the low plasticity clays the addition of

the non-linear elastic model enables a good representation of the stiffness decay during the early stages of shearing.

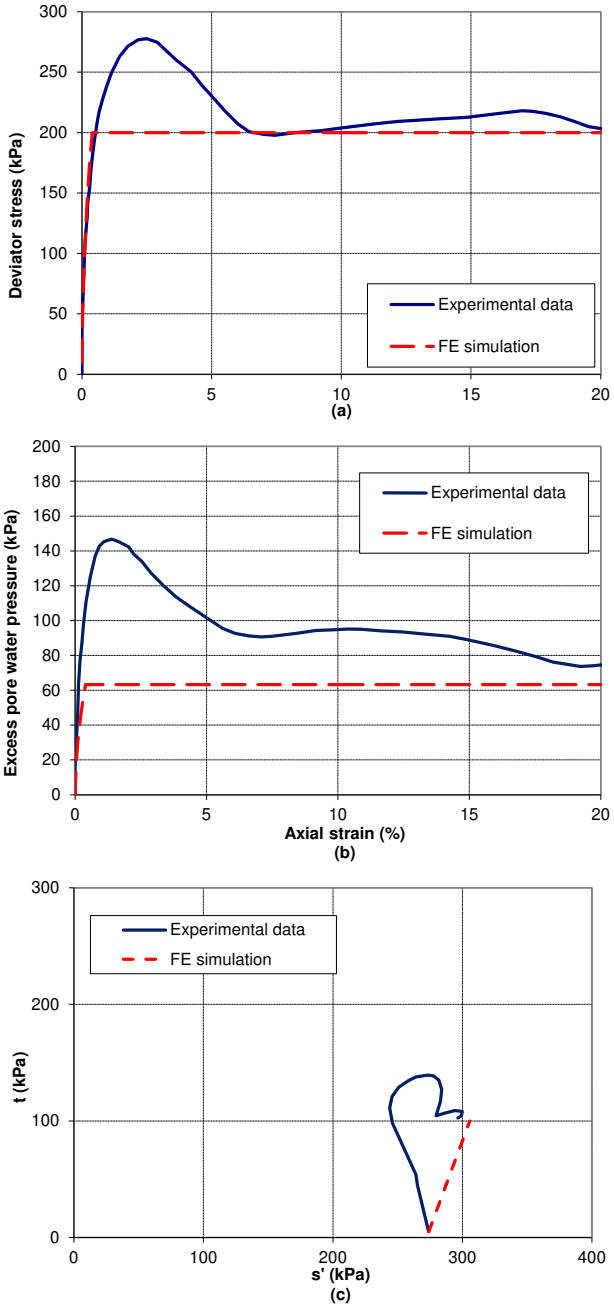

Figure 35. Comparison of experimental and simulated response for a CAUc test on stiff plastic clay – Channel infill material from neighbouring site (from Grammatikopoulou et al., 2017)

The modelling of stiff plastic clays in relation to the response of monopiles to lateral loading has also been investigated in the recent PISA2 research project and some findings from this study are reported by Zdravkovic et al. (2021). PISA2 studied the response of London Clay, a stiff marine sedimentary overconsolidated clay, with PI ≈ 35-50%. As Zdravkovic et al. (2021) note, the two main differences in the mechanical response of London Clay and the low plasticity Cowden Till are i) the brittle response of London Clay during shearing and ii) its markedly anisotropic shear stiffness with $G_{hh} > G_{hv}$ (Gasparre et al., 2007).

Zdravkovic et al. (2021) studied the effect of the brittleness in strength on the undrained response of laterally loaded monopiles in London Clay and found that this has a negligible effect, with only marginal differences (between softening and non-softening analyses) at intermediate horizontal displacement levels.

As such, Zdravkovic et al. (2021) investigated the use of the same modelling framework as for the low plasticity clays, but, in this case, the hardening on the dry side of critical, obtained with the MCC model, was suppressed. This was achieved by using a modified plastic potential, which does not allow plastic volumetric straining, once the Hvorslev yield surface is invoked.

In addition, the model was further extended to include the modelling of the anisotropic non-linear pre-yield stiffness of London Clay.

The stiffness of natural London Clay from London's Heathrow Terminal 5 has been studied using a combination of advanced triaxial, hollow cylinder apparatus (HCA), bender element and resonant column tests (Gasparre et al., 2007). The study showed that cross anisotropy can be assumed to describe the stiffness of this material at very small strains. Figure 36 shows the stiffness properties derived by the study; this shows that at very small strains there is a factor of approximately 2 between G_{hh} and G_{vh}.

The evolution of stiffness anisotropy with strain of four UK stiff sedimentary clays, including London Clay, was studied by Brosse et al. (2017) using the results of advanced triaxial, HCA, bender element and resonant column tests. Figure 37 presents the $E_{u,v}$, $E_{u,h}$ and G_{vh} decay curves calculated on the basis of the results of HCA tests, by assuming cross anisotropy, for five orientations, α_f, of the major principal stress axis (in relation to the vertical). This shows that the ratio of secant Young's moduli $E_{u,h}/E_{u,v}$, and hence the degree of anisotropy, changes with both strain and α_f.

As discussed by Zdravkovic et al. (2021), the stiffness anisotropy of London Clay is reflected in the stress paths of triaxial tests, which are inclined to the left, as shown in Figure 38 (in which the laboratory test data are denoted as T-5, T-11 and T-17). If isotropic elasticity applied, then the stress path would have been vertical, in the q-p' stress space. Figure 38 also shows the predictions of Zdravkovic et al. (2021) using the modified MCC model described above, when assuming a stiffness anisotropy which i) remains constant with strain (T-5 A, T-11 A and T-17 A) and ii) reduces with strain (T-5 Av, T-11 Av and T-17 Av). It can be seen that the latter captures well the measured stress paths of the triaxial compression tests.

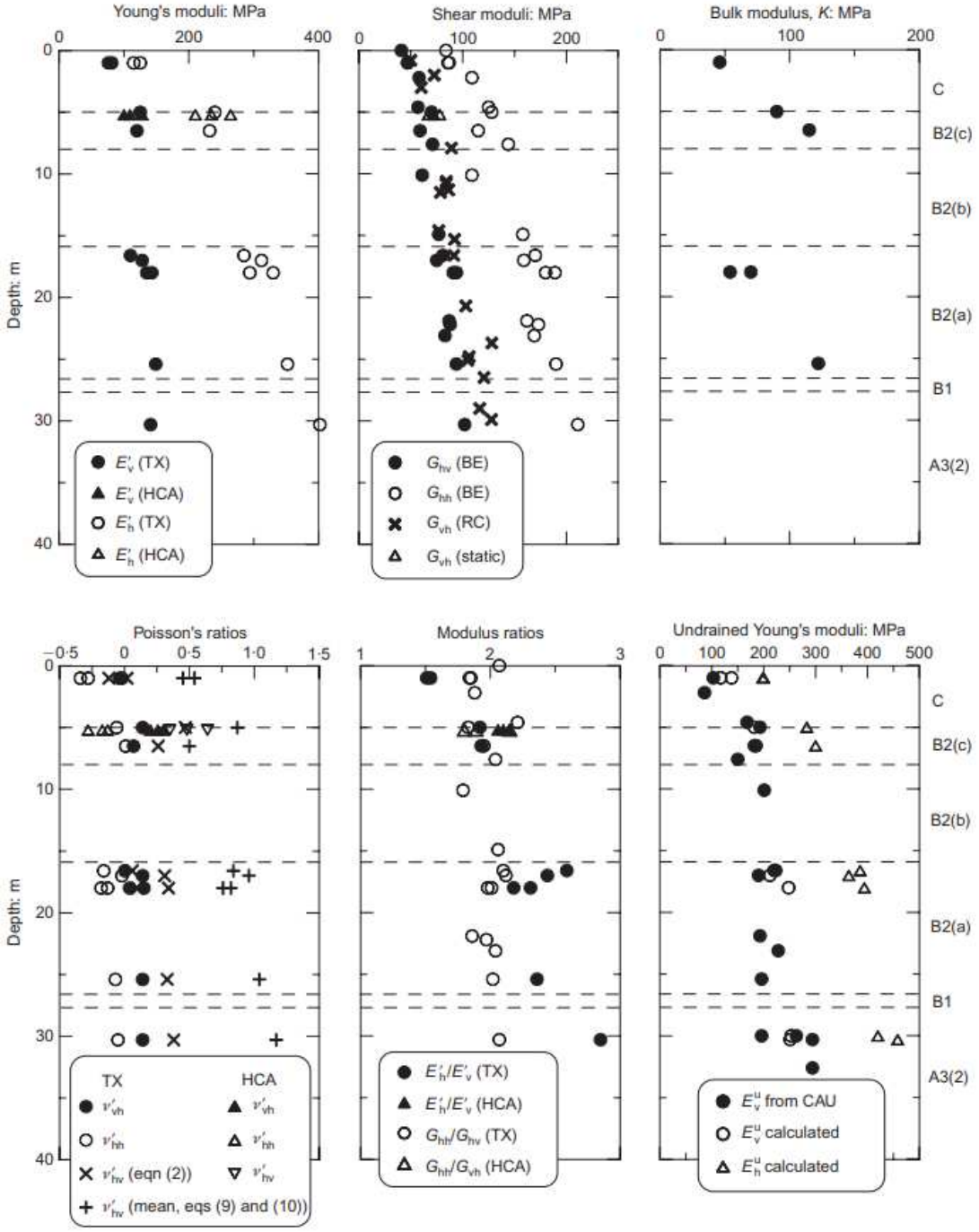

Figure 36. Stiffness parameters of London Clay at small strains (from Gasparre et al., 2007)

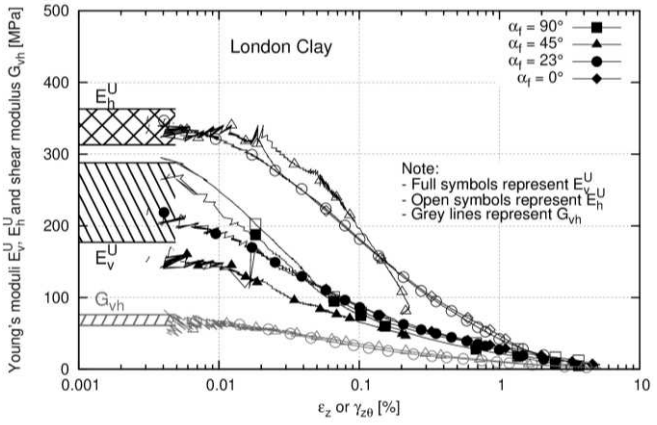

Figure 37. Secant $E_{u,h}$, $E_{u,v}$ and G_{vh} degradation curves from HCA stress path tests (from Brosse et al., 2017)

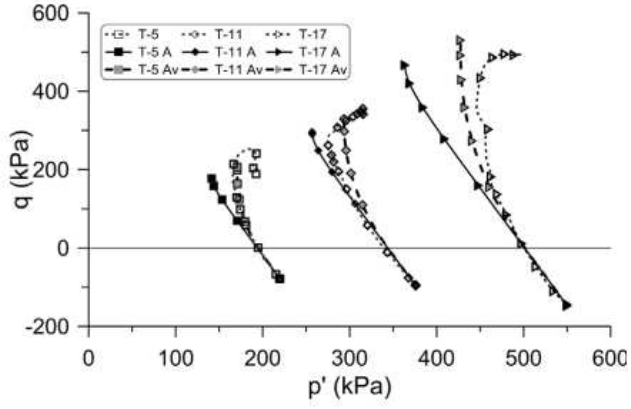

Figure 38. Effective stress paths of London Clay (from Zdravkovic et al., 2021)

A challenge in applying the above in practice (as also discussed by Zdravkovic et al. (2021)) is the difficulty in establishing the full extent of stiffness anisotropy of a given material, on the basis of, even advanced, commercial ground investigations. For example, although it is possible to measure $E_{u,v}$ and its degradation with strain in triaxial tests and G_{hv}, G_{vh} and G_{hh} with bender elements, and possibly in-situ seismic tests, it is very difficult to establish the variation of these parameters with increasing strain levels, as this requires carefully conducted HCA testing, which is rarely included in commercial investigations.

Moreover, an additional challenge with offshore clay formations, like the channel infill materials shown in Figures 34 and 35, is associated with their variable depositional environments and complex geological histories. As such, unlike stiff sedimentary clays, which may have a relatively well-known depositional and geological history, the stiffness anisotropy of offshore clays may be variable and may not be as well described by cross-anisotropy.

4 SUMMARY AND CONCLUSIONS

This paper presents an overview of the authors' experience in the application of constitutive models to simulate the response of soils that are commonly encountered in offshore wind farm sites.

The work presented emphasises the need to: i) characterise accurately the soil formations encountered, on the basis of detailed interpretations of high-quality ground investigations (comprising in-situ and advanced laboratory tests), ii) choose appropriate sophisticated constitutive models which can describe the key facets of the soils' response, iii) calibrate the models, on the basis of the high quality ground investigation information from across the wind farms, to accurately replicate the measured soil response at an element level and iv) apply the models in 3D FE analyses of monopile foundations, on the basis of location specific information.

The paper highlights the difficulties faced when applying the above in sand and clay formations, which is particularly challenging for offshore wind farm sites, due to the greater variability of the materials encountered as compared to, normally smaller, onshore sites.

Although the paper discusses the application of the constitutive models in the analysis of monopile foundations, the findings presented in relation to the calibration of the constitutive models and their ability to simulate the soils' response at an element level are not limited to this geotechnical problem.

4.1 Modelling sands

The first part of the paper examines the application of two elasto-plastic constitutive models in simulating the response of sands of varying density, i.e.:

i) a state parameter-dependent constitutive model based on the Mohr-Coulomb failure criterion (Taborda et al., 2018)

ii) a strain softening Mohr Coulomb model developed by Potts et al. (1990), and previously used by the authors in the design of monopile foundations.

Both models are combined with the non-linear elastic model IC.G3S (Taborda et al., 2016).

The paper presents the calibration of the two models to high-quality in-situ and laboratory test data for two sand formations encountered at a sand dominated offshore wind farm site and their application in the 3D FE analysis of an example monopile foundation, on the basis of CPT correlations at the corresponding WTG location.

The calibration of the state parameter-dependent model demonstrates the difficulties in establishing a unique position of the CSL, on the basis of laboratory test data. Consequently, the paper investigates two calibrations of the model: Calibration 1, which adopts a unique position of the CSL, on the basis of testing relatively loose samples, and Calibration 2, which adopts a CSL whose position depends on relative density. The following comments can be made:

- Calibration 1 is consistent with the theoretical framework of critical state soil mechanics but results in an overestimation of the dilative strains measured in CID tests conducted at medium to high densities.
- Calibration 2 does not agree strictly with the critical state framework but is a practical way of reproducing the dilative response measured in CID tests of dense and very dense samples, whilst acknowledging the limitations of these tests in relation to strain localisation and shear banding.
- Both calibrations reproduce well the measured peak and post-peak stress-strain response of the two sand formations encountered at the OWF.
- Comparisons of single element FE simulations with laboratory results of CID tests, at a variety of stress states and densities, show that both calibrations of the state parameter dependent model can reproduce well the dependence of the sands' response on stress state and density.

The calibration of the strain-softening Mohr-Coulomb model shows that:

- By allowing the angles of shearing resistance and dilation to vary with strain it is possible to capture the peak and post-peak stress-strain and dilative response measured in relevant triaxial tests. However, the input parameters need to be varied on the basis of density and stress levels. This is in contrast to the state parameter-dependent model, in which a single set of parameters can be used.
- Comparisons of single element FE simulations with CID laboratory test results for a variety of stress states and densities, highlights that although

the model generally predicts well the measured response, it does not capture the peak and volumetric response of some samples with the chosen model parameters. In general, the model is not as versatile as the state parameter-dependent model and, even if different input parameters are adopted, it is not straightforward to capture the subtleties of the sands' dependence on both stress state and density.

Comparisons of the measured and simulated stiffness-strain response for the advanced triaxial tests that were equipped with local instrumentation show that:

- The non-linear elastic model IC.G3S captures very well the dependence of both sands' stiffness on density, stress-state and strain level.

Comparisons of the models' predictions in the 3D FE analysis of an example monopile foundation, subjected to lateral loading, show the following:

- The two calibrations of the state parameter-dependent model and the strain-softening Mohr-Coulomb model predict practically the same initial monopile response. This is not surprising as all three analyses use the same non-linear elastic model.
- There is a substantial difference in the overall predicted monopile response, with the state parameter-dependent model Calibration 1 resulting in a significantly higher lateral load carrying capacity than Calibration 2. This would also affect any soil-reaction curves extracted from the analyses and highlights the significance of the assumptions in relation to the critical state line.
- The predictions of the strain-softening Mohr-Coulomb model are closer to the predictions of Calibration 2 of the state parameter-dependent model. This is in line with the fact that Calibration 2 aimed to reproduce the volumetric response measured in the CID tests, on which the Mohr-Coulomb model calibration was based.
- However, it is noted that in the chosen example monopile location, the sands' densities are practically constant at the depths relevant to the monopile analysis. As such, larger differences in predicted monopile response and lateral capacity between the two elasto-plastic models is likely to apply to locations with varying sand density.

In addition to the above, the paper presented a study on the choice of parameters for the Mohr-Coulomb model highlighting the significance of both the assumed angle of shearing resistance and the angle of dilation.

4.2 Modelling stiff clays

The second part of the paper presents the modelling of stiff clays. The paper emphasises the need to establish the variability of any clay formations, with particular focus on plasticity, as it affects significantly the clays' shear response. This is particularly relevant for offshore wind farm sites, as varying depositional environments and complex geological histories, in combination with the sizes of the sites, can result in a variety of clay formations and significant variability within each clay formation.

The following comments can be made:

- Individual clay formations, such as the channel infill materials form a North Sea OWF, can show large variations in plasticity index. This can result in a variable response to undrained shearing ranging from brittle for high plasticity materials to ductile for low plasticity materials.
- As it is not always clear from CPT data (often the only piece of information available for each WTG location) whether the stiff clays encountered are of low or of high plasticity, it is important that the available laboratory tests are carefully reviewed before choosing what type of constitutive model is used to best represent the clay deposits encountered. If the variability of the material is found to be significant, then a conservative approach would need to be adopted.
- The enhanced Modified Cam Clay model, used in the PISA project to simulate the response of Cowden Till, has been shown to reproduce well the ductile response, measured in undrained shearing, of low plasticity glacial till deposits, encountered in Northern European offshore wind farms.
- For low plasticity clays, the paper demonstrates how the enhanced MCC model can be applied to a specific monopile location by adjusting the assumed yield stress ratio profile to match the undrained strength obtained on the basis of CPT correlations.
- Stiff plastic clays are more difficult to model as they exhibit non-critical state conditions often associated with post-peak brittleness. While simple models of the Tresca type can be combined with non-linear elastic models to capture some of the critical aspects of behaviour, they have obvious limitations and require careful choices of appropriate model parameters.
- Another feature of many clays that influences the behaviour of laterally loaded monopiles, is stiffness anisotropy, as demonstrated by Zdravkovic et al. (2021), who used the same modelling framework as in the PISA project but with further modifications to simulate the response of London Clay, i.e. a stiff sedimentary plastic clay with marked cross-anisotropic stiffness.
- However, there are significant challenges of including stiffness anisotropy in modelling the response of stiff clay formations when analysing laterally loaded monopiles for a specific offshore wind farm. This is because i) it is difficult to assess the full extent of stiffness anisotropy on the basis

of, even advanced, commercial tests, and ii) the often complex depositional environments and geological history, may lead to significant variations in stiffness anisotropy and/or the inability to describe them with cross-anisotropy.

4.3 Final remarks

This paper demonstrates the need for the constitutive modeller to i) have a deep understanding of soil characterisation and interpretation of soil testing (laboratory and in-situ) and ii) be fully conversant with the constitutive models employed and their implementation in the particular FE software they are using. This is critical to enable a sound understanding of the advantages and limitations of any particular chosen model, as well as the impact of individual model parameters on the resulting model behaviour.

Even so, the derivation of model parameters and associated model calibration on the basis of laboratory and in-situ test data, can often be challenging owing to limitations in the available data, even in sophisticated high-quality investigations, and inherent variability of the materials encountered, especially in the case of offshore wind farms which tend to cover large areas. In addition, it has to be appreciated that not all stress states, stress paths, etc. encountered in the FE analyses of a given boundary value problem, especially when employing 3D analyses, will be covered by available laboratory test data. As such it is of paramount importance that continuous comparisons between FE predictions and field measurements of geotechnical problems and/or field tests are undertaken in order to check the suitability of the numerical models and the appropriateness of the modelling assumptions.

5 ACKNOWLEDGMENTS

The authors would like to thank Ørsted and RWE for permission to publish the laboratory and in-situ test data from the offshore wind farms and particularly Dr Vasileios Avgerinos and Mr Andy Barwise, with whom they cooperated on these offshore wind farm projects.

6 REFERENCES

Baldi, G., Belloti, R., Ghionna, V., Jamiolkowski, M., Pasqualini, E. 1986. Interpretation of CPT's and CPTU's ; 2nd Part : drained penetration of sands. *Proceedings of 4th Int. Geotechnical Seminar*, Singapore, 143-156.

Been, K. Jefferies, M.G. 1985. A state parameter for sands, *Géotechnique* **35 (2)**, 99–112.

Brosse, A., Hosseini Kamal, R., Jardine, R.J., Coop, M.R. 2017. The shear stiffness characteristics of four Eocene-to-Jurassic UK stiff clays, *Géotechnique* **67 (3)**, 242–259.

Burd, H.J., Taborda, D.M.G., Zdravković, L., Abadie, C.N., Byrne, B.W., Houlsby, G.T., Gavin, K.G., Igoe, D., Jardine, R.J., Martin, C.M., McAdam, R.A., Pedro, A.M.G., Potts D.M. 2020. PISA design model for monopiles for offshore wind turbines: application to a marine sand, *Géotechnique* **70 (11)**, 1048–1066.

Byrne, B.W., Houlsby, G.T., Burd, H.J., Gavin, K.G., Igoe, D., Jardine, R.J., Martin, C.M., McAdam, R.A., Potts D.M., Taborda, D.M.G., Zdravković, L. 2020. PISA design model for monopiles for offshore wind turbines: application to a stiff glacial clay till, *Géotechnique* **70 (11)**, 1030–1047.

Chu, J. 1995. An experimental examination of the critical state and other similar concepts for granular soils, *Canadian Geotechnical Journal* **32**, 1065-1075.

Dafalias, Y.F., Manzari, M.T. 2004. Simple plasticity sand model accounting for fabric change effects. *ASCE Journal of Engineering Mechanics* **130(6)**, 622-634.

Day, R.A., Potts, D.M. 1994. Zero thickness interface elements – numerical stability and application. *International Journal for Numerical and Analytical Methods in Geomechanics* **18(10)**, 689-708.

Desrues, J., Chambon, R., Mokni, M., Mazerolle, F. 1996. Void ratio evolution inside shear bands in triaxial specimens studied by computed tomography, *Géotechnique* **46 (3)**, 529–546.

Gasparre, A., Nishimura, S., Anh-Minh, N., Coop, M. R., Jardine, R. J., 2007. The stiffness of natural London Clay, *Géotechnique* **57(1)**, 33–47.

Grammatikopoulou, A., Schroeder, F.C., Brosse, A.M., Andersen, K.W., Potts, D.M. 2017. On the use of constitutive models in numerical analyses of offshore structures. *Smarter Solutions for Future Offshore Developments: Proceedings, 8th International Offshore Site Investigation and Geotechnics Conference, London*, 423-420. London, UK.

Grammatikopoulou, A., Schroeder, F.C., Pedone, G., Brosse, A.M., Sørensen, T., Taborda, D.M.G., Potts, D.M. 2020. 3D Finite Element Analysis of monopiles and its application in offshore wind farm design. *ISFOG 2020: Proceedings, 4th International Symposium on Frontiers in Offshore Geotechnics, Austin Texas* (Eds. Westgate, Z.), 1221-1230. Deep Foundations Institute.

Grammatikopoulou, A., Zdravković, L., Potts, D.M. 2007. The effect of the yield and plastic potential surfaces on the failure height of an embankment, *Géotechnique* **57(10)**, 795–806.

Jamiolkowski M.B., Lo Presti, D.C.F, Manassero, M. 2003. Evaluation of relative density and shear strength of sands from cone penetration tests (CPT) and flat dilatometer (DMT), *Soil Behaviour and Soft Ground Construction*, Eds. J.T. Germain, T.C. Sheahan and R.V. Whitman, ASCE, GSP 119, 201-238.

Jefferies, M.G. 1993. Nor-Sand: a simple critical state model for sand, *Géotechnique* **43(1)**, 91-103.

Jefferies, M.G., Been, K. 2006. *Soil liquefaction: a critical state approach*. Boca Raton: CRC Press.

Lambe, T.W. 1973. Predictions in soil engineering, *Géotechnique* **23 (2)**, 149–202.

Li, X.S., Wang, Y. 1998. Linear representation of steady-state line for sand, *Journal of Geotechnical and Geoenvironmental Engineering* **124 (12)**, 1215–1217.

Lo, Presti D.C.F., Pallara, O., Lancellotta, R., Armandi, M., Maniscalco, R. 1993. Monotonic and cyclic loading behavior of two sands at small strains, *Geotechnical Testing Journal* **16(4)**, 409–424.

Papadimitriou, A.G. Bouckovalas, G.D. 2002. Plasticity model for sand under small and large strains: a multiaxial formulation, *Soil Dynamics and Earthquake Engineering* **22**, 191–204.

Pestana, J.M., Whittle, A.J. 1999. Formulation of a unified constitutive model for clays and sand, *International Journal for Numerical and Analytical Methods in Geomechanics* **23**, 1215-1243.

Potts, D.M., Dounias, G.T., Vaughan P.R. 1990. Finite element analysis of progressive failure of Carsington embankment, *Géotechnique* **40(1)**, 90–101.

Potts, D.M., Gens, A. 1984. The effect of the plastic potential in boundary value problems involving plane strain deformation, *International Journal for Numerical and Analytical Methods in Geomechanics* **8(3)**, 259-286

Potts, D.M., Zdravković L. 1999. *Finite element analysis in geotechnical engineering: Theory; Vol.1*, Thomas Telford.

Rix, G.J., Stoke, K.H. 1992. Correlation of initial tangent modulus and cone resistance. *Proceedings of the International Symposium on Calibration Chamber Testing, Potsdam, New York,* 351-62, Elsevier.

Roscoe, K. H., Burland, J. B. 1968. On the generalized stress–strain behavior of wet clay. In *Engineering plasticity* (Eds: J. Heyman and F. A. Leckie), 535–609. Cambridge University Press, Cambridge, UK.

Schroeder, F.C., Day, R.A., Potts, D.M., Addenbrooke, T.I. 2007. A quadrilateral isoparametric shear deformable shell element for use in soil-structure interaction problems, *ASCE International Journal of Geomechanics* **7(1)**, 44-52.

Schroeder, F.C., Grammatikopoulou, A., Barwise, A., MacKinnon, S., Jardine, R.J., Potts, D.M. 2020. The use of numerical analysis to aid the design of monopile foundations for a North Sea offshore wind farm. *ISFOG 2020: Proceedings, 4th International Symposium on Frontiers in Offshore Geotechnics, Austin Texas* (Eds. Westgate), Z., 1566-1575. Deep Foundations Institute.

Summersgill, F.C., Kontoe, S., Potts, D.M. 2017a. On the use of nonlocal regularisation techniques in slope stability problems, *Computers and Geotechnics* **82**, 187–200.

Summersgill, F.C., Kontoe, S., Potts, D.M. 2017b. Critical assessment of non-local strain-softening methods in biaxial compression, *ASCE International Journal of Geomechanics* **17(7)**, 1–14.

Taborda, D.M.G., Potts, D.M., Zdravković L. 2016. On the assessment of energy dissipated through hysteresis in finite element analysis, *Computers and Geotechnics* **71**, 180–194.

Taborda, D.M.G., Potts, D.M., Zdravković L., Pedro, A.M.G. 2018. Incorporating the state parameter into a simple constitutive model for sand. *Proceedings of 9th European Conference on Numerical Methods in Geotechnical Engineering, Porto,* 327-334.

Taborda, D.M.G., Zdravković L., Kontoe, S., Potts, D.M. 2014. Computational study on the modification of a bounding surface plasticity model for sands, *Computers and Geotechnics* **59**, 145–160

Taborda, D.M.G., Zdravković, L., Potts D.M., Burd, H.J., Byrne, B.W., Gavin, K.G., Houlsby, G.T., Jardine, R.J., Liu, T., Martin, C.M., McAdam, R.A. 2020. Finite-element modelling of laterally loaded piles in a dense marine sand at Dunkirk, *Géotechnique* **70 (11)**, 1014–1029.

Tsiampousi, A., Zdravković, L., Potts, D.M. 2013. A new Hvorslev surface for critical state type unsaturated and saturated constitutive models, *Computers and Geotechnics* **48**, 156–166.

Van Eekelen, H.A.M. 1980. Isotropic yield surfaces in three dimensions for use in soil mechanics, *International Journal for Numerical and Analytical Methods in Geomechanics* **4**(1), 89–101.

Zdravkovic, L., Jardine, R.J., Taborda, D.M.G., Abadias, D., Burd, H.J., Byrne, B.W., Gavin, K.G., Houlsby, G.T., Igoe, D.J.P., Liu, T., Martin, C.M., McAdam, R.A., Muir Wood, A., Potts D.M., Skov Gretlund, J., Ushev, E. 2020a. Ground characterisation for PISA pile testing and analysis, *Géotechnique* **70 (11)**, 945–960.

Zdravkovic, L., Potts D.M., Taborda, D.M.G. 2021. Integrating laboratory and field testing into advanced geotechnical design, *Geomechanics for Energy and the Environment* **27**, 1–21.

Zdravković, L., Taborda, D.M.G., Potts, D.M., Abadias, D., Burd, H.J., Byrne, B.W., Gavin, K.G., Houlsby, G.T., Jardine, R.J., Martin, C.M., McAdam, R.A., Ushev, E. 2020b. Finite-element modelling of laterally loaded piles in a stiff glacial clay till at Cowden, *Géotechnique* **70 (11)**, 999–1013.

APPENDIX A: SIMULATIONS – STATE PARAMETER-DEPENDENT MODEL

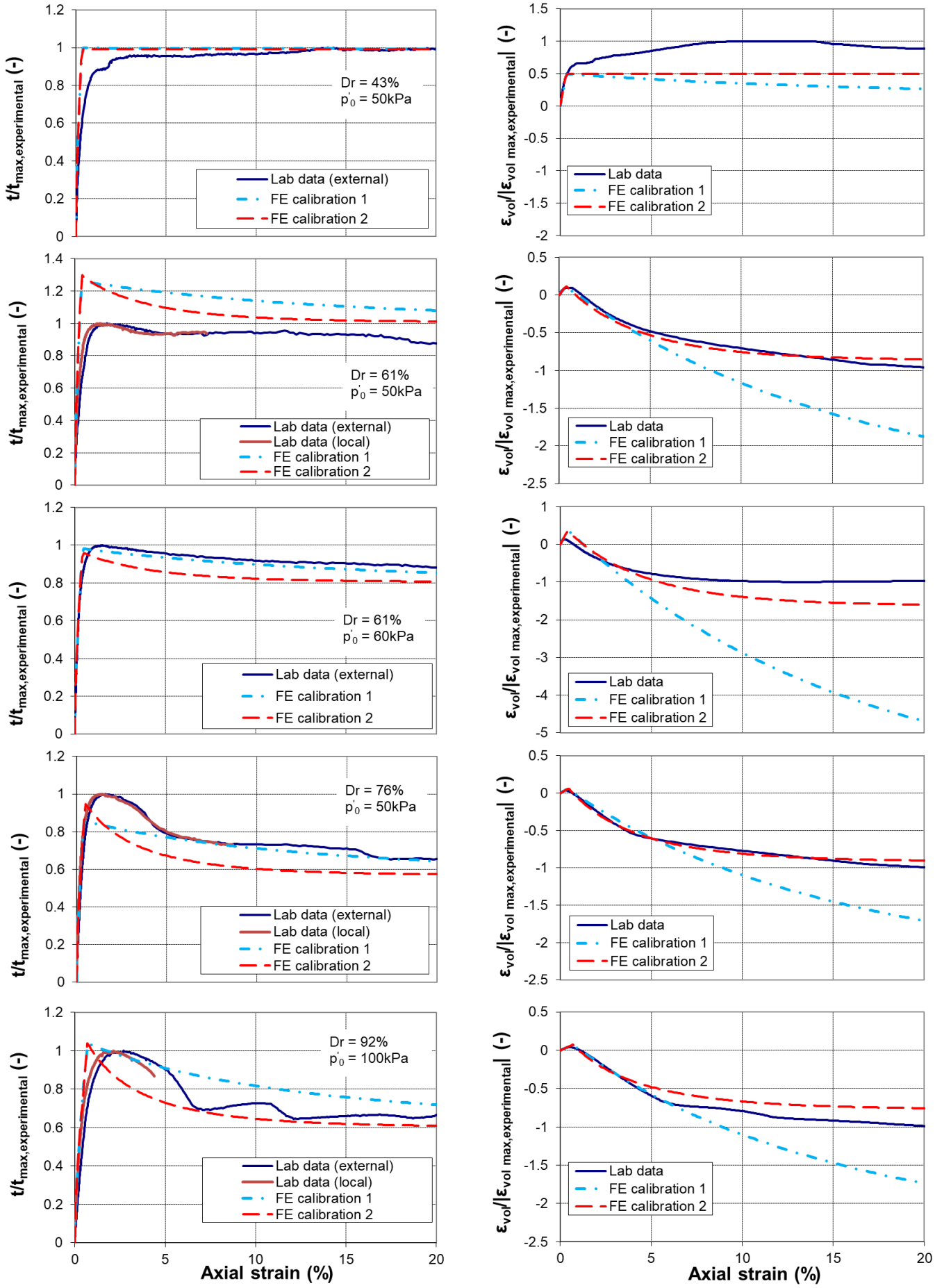

Figure A1: Comparison of experimental and simulated response for Sand A

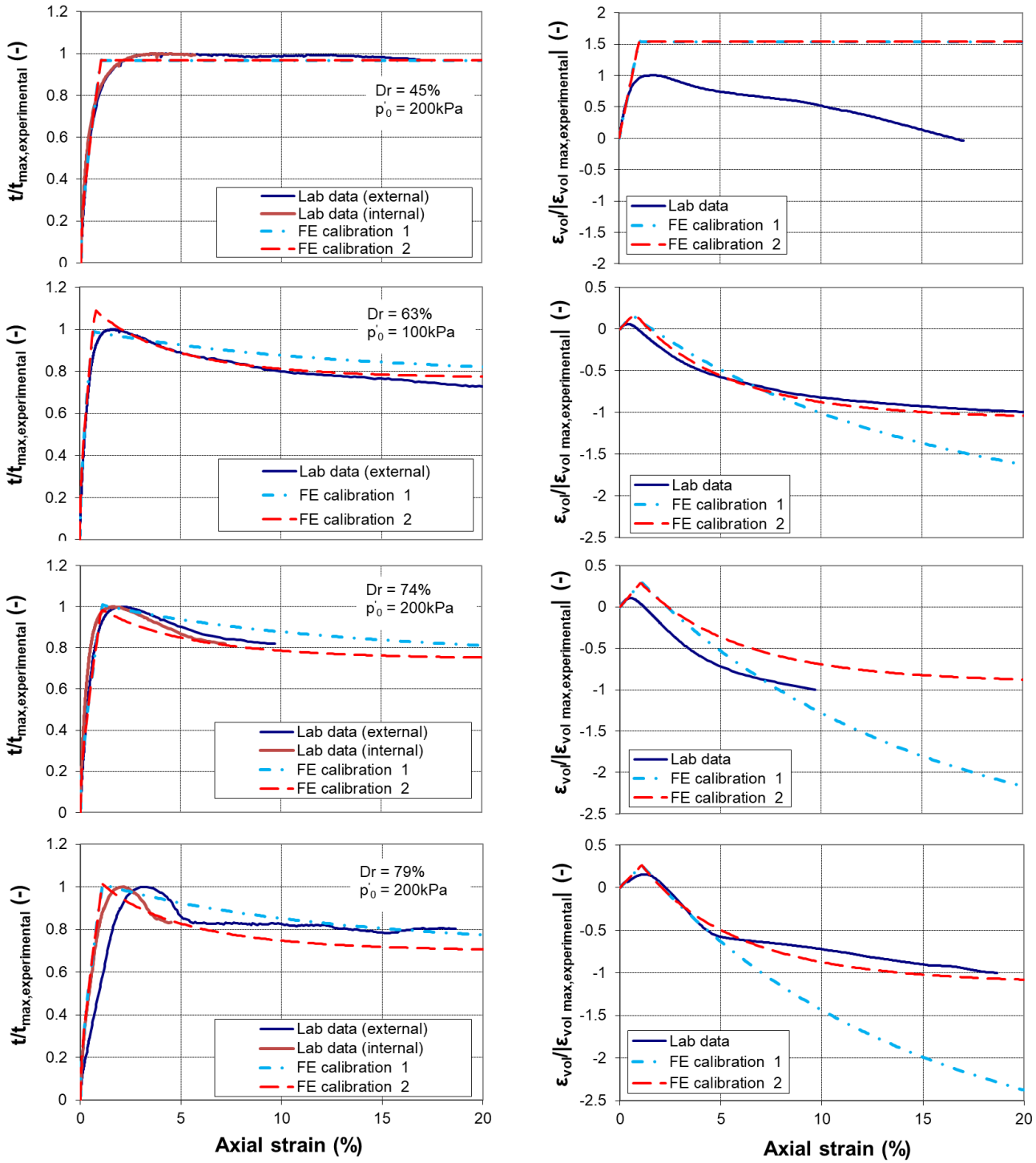

Figure A2: Comparison of experimental and simulated response for Sand B and D_r = 40-80%

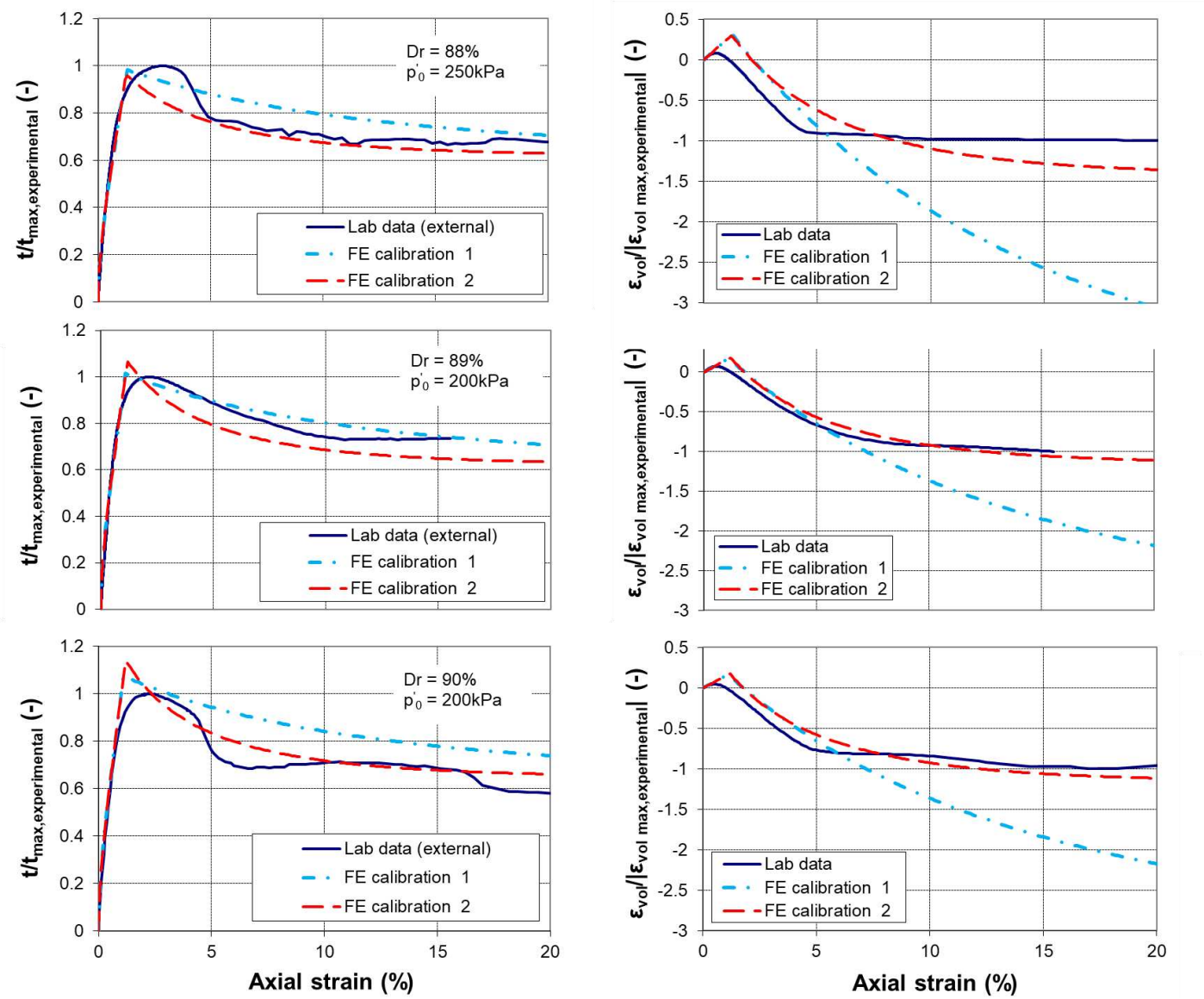

Figure A3: Comparison of experimental and simulated response for Sand B and $D_r \approx 90\%$

APPENDIX B: SIMULATIONS – STRAIN-SOFTENING MOHR-COULOMB MODEL

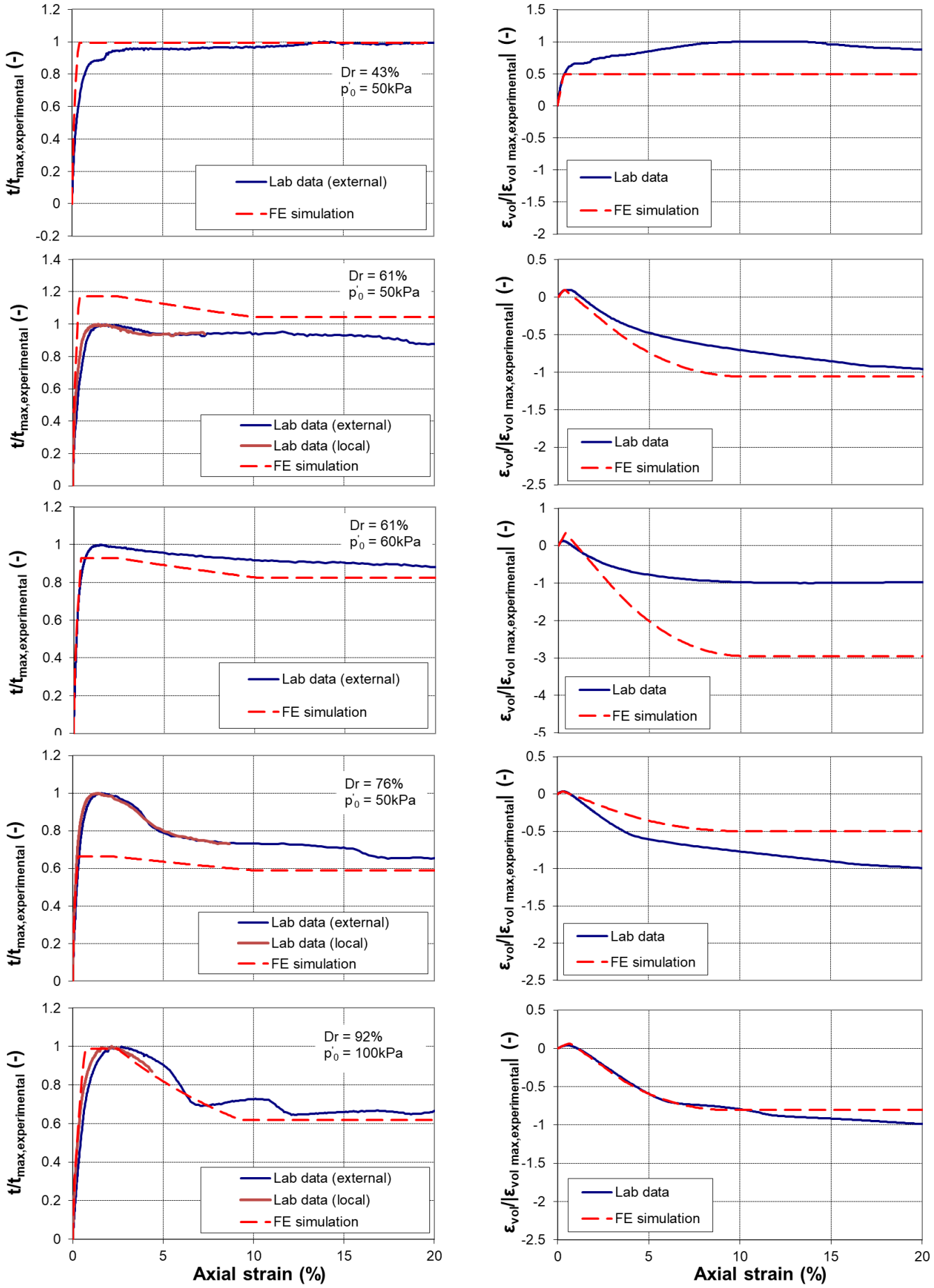

Figure B1: Comparison of experimental and simulated response for Sand A

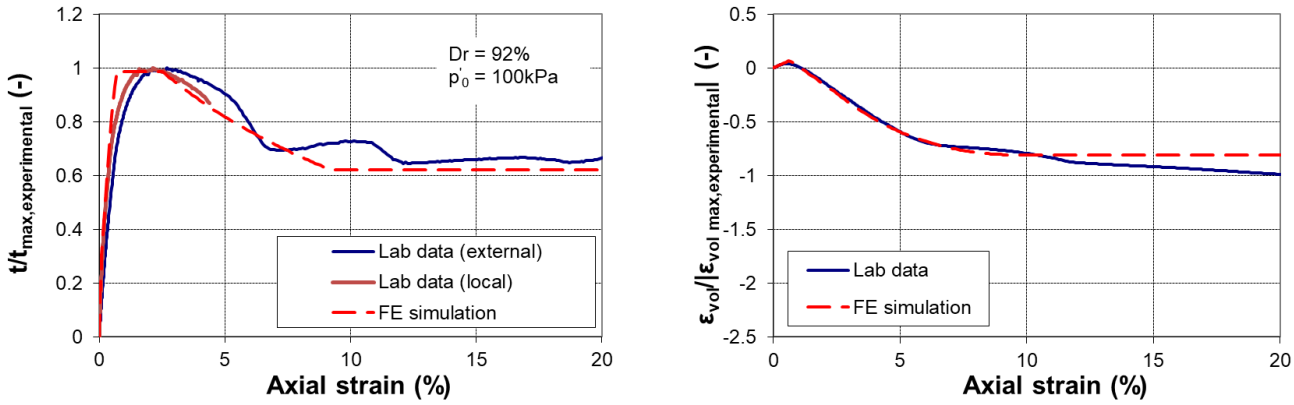

Figure B2: Comparison of experimental and simulated response for Sand A and D_r = 92%

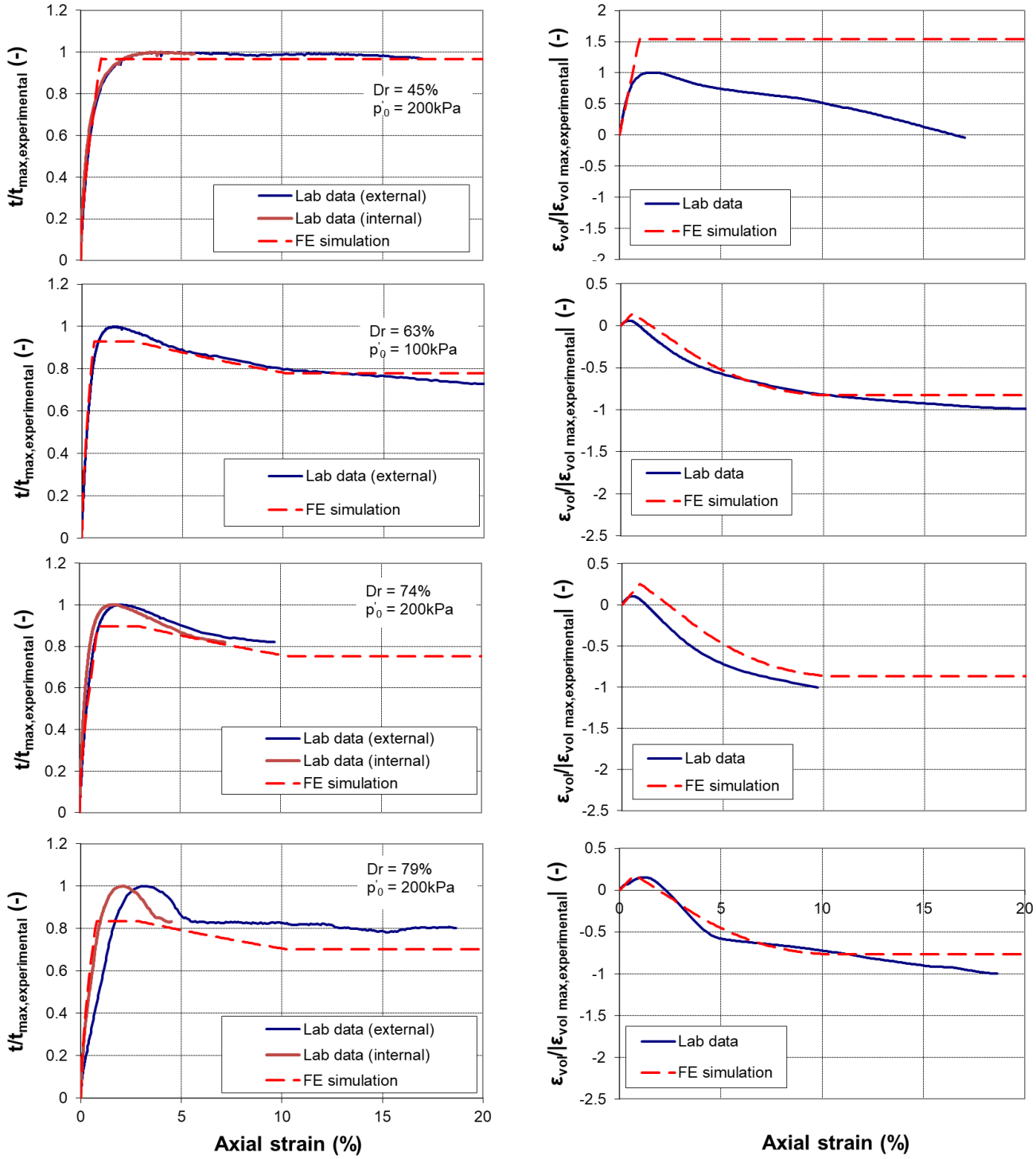

Figure B2: Comparison of experimental and simulated response for Sand B and D_r = 40-80%

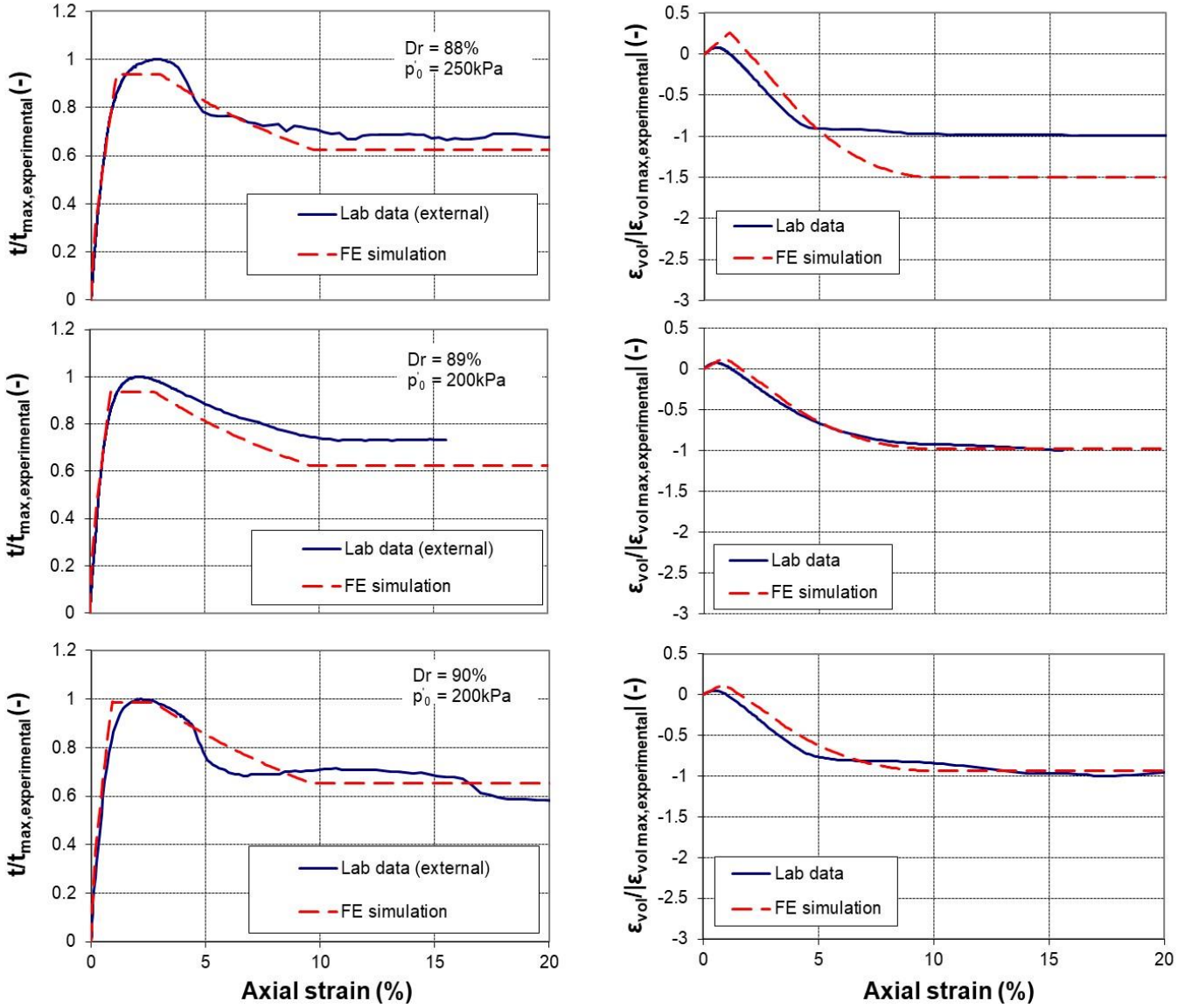

Figure B3: Comparison of experimental and simulated response for Sand B and $D_r \approx 90\%$

APPENDIX C: SIMULATIONS – STIFFNESS-STRAIN RESPONSE

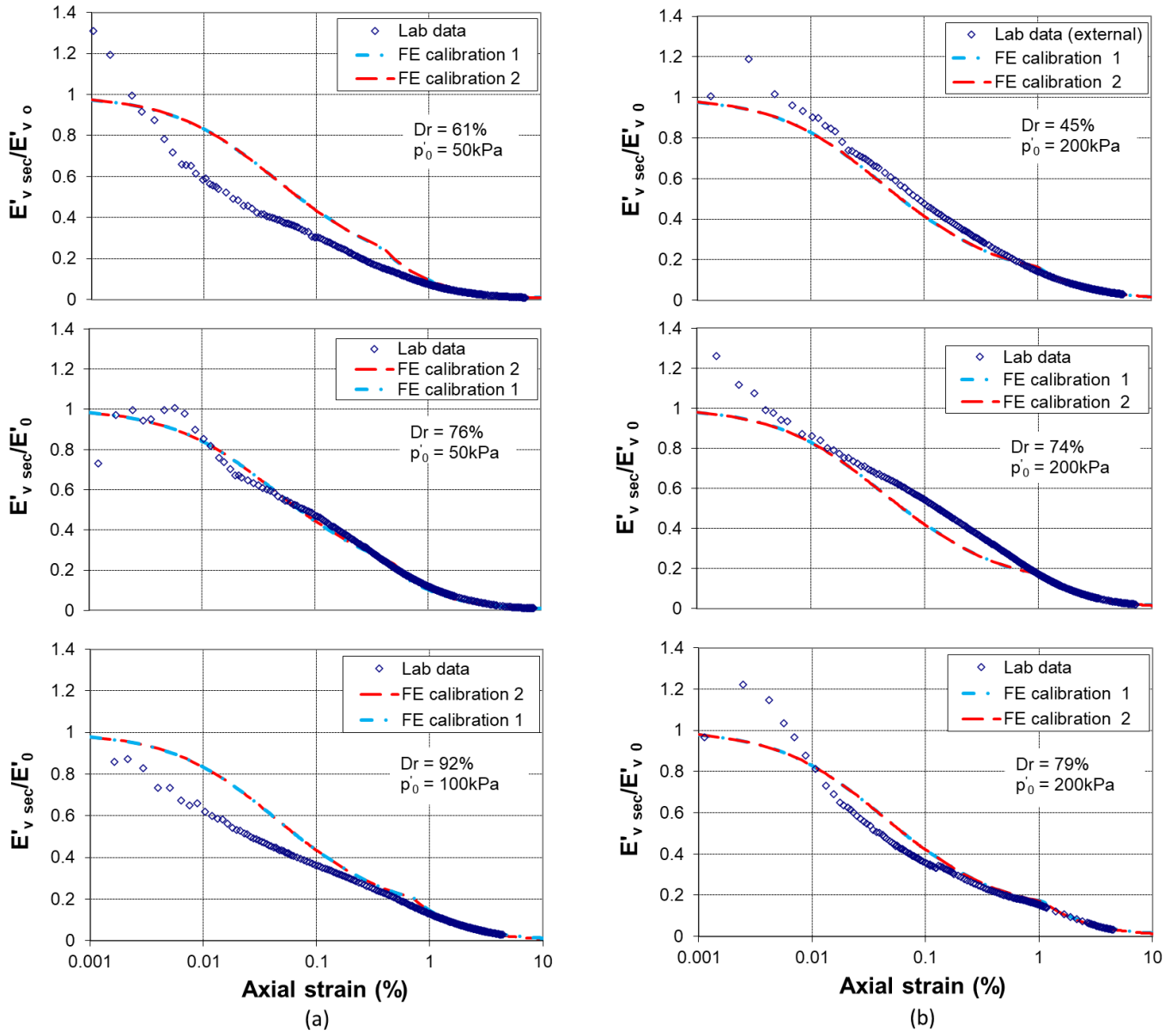

Figure C1: Comparison of experimental and simulated stiffness-strain response for a) Sand A b) Sand B